SCUOLA
NORMALE
SUPERIORE

Faculty of Science

Course in Nanoscience

XXXII cycle

Fluorescence lifetime microscopy unveils the nanoscale organization of liposomal Doxorubicin

SSD **FIS/07**

Candidate
dr. Paolo Maria Tentori

Advisor
Prof. Francesco Cardarelli

Academic year 2022/2023

Content

List of Figures

List of Articles

Articles included in this Thesis:

1 **Paolo Tentori**, Giovanni Signore, Andrea Camposeo, Annalisa Carretta, Gianmarco Ferri, Pasqualantonio Pingue, Stefano Luin, Daniela Pozzi, Enrico Gratton, Fabio Beltram, Giulio Caracciolo and Francesco Cardarelli. *Fluorescence lifetime microscopy unveils the supramolecular organization of liposomal Doxorubicin*. (Communication) Nanoscale, May 2022, 14, 8901-8905. doi: 10.1039/D2NR00311B

2 Erica Quagliarini, Riccardo Di Santo, Daniela Pozzi, **Paolo Tentori**, Francesco Cardarelli, Giulio Caracciolo. *Mechanistic Insights into the Release of Doxorubicin from Graphene Oxide in Cancer Cells.* Nanomaterials (Basel). 2020 Jul 29;10(8):1482. doi: 10.3390/nano10081482.

3 Giulio Caracciolo, Sara Palchetti, Luca Digiacomo, Riccardo Zenezini Chiozzi, Anna Laura Capriotti, Heinz Amenitsch, **Paolo Tentori**, Valentina Palmieri, Massimiliano Papi, Francesco Cardarelli, Daniela Pozzi, and Aldo Laganà. *Human Biomolecular Corona of Liposomal Doxorubicin: The Overlooked Factor in Anticancer Drug Delivery*. ACS Appl. Mater. Interfaces 2018, 10, 27, 22951–22962 https://doi.org/10.1021/acsami.8b04962

Patent

1 **Paolo Tentori**, Francesco Cardarelli, Giulio Caracciolo, Daniela Pozzi, Fabio Beltram. Numero domanda: 102020000026699 *Determinazione dell'organizzazione supramolecolare di molecole incapsulate tramite analisi del tempo di vita della luminescenza*

Articles not included in this Thesis:

1 Luca Digiacomo, Francesca D'Autilia, William Durso, **Paolo Tentori**, Giulio Caracciolo & Francesco Cardarelli. *Dynamic fingerprinting of sub-cellular nanostructures by image mean square displacement analysis*. Scientific Reports volume 7, Article number: 14836 (2017) 01 November 2017 https://doi.org/10.1038/s41598-017-13865-4

Nomenclature

FLIM: Fluorescence lifetime imaging microscopy; an imaging technique for producing an image based on the differences in the exponential decay rate of the fluorescence from a fluorescent sample. It can be used as an imaging technique in confocal microscopy.

DOX: free form of Doxorubicin Hydrochloride, chemotherapy medication used to treat cancer.

DOX®: PEGylate Liposomal formulation of DOX, characterized by a size of around 80-90 nm.

DOX_c: Nanorod crystal-like structure of DOX. The formation of this drugs is the result of interaction of ionized DOX with the $SO4^{2-}$anions forming an insoluble salt.

DOX_b: DOX conjugated with the lipidic bilayer of the liposome.

DLN: DOX®-like nanoparticles; resulting by using a low concentration of ammonium sulfate during the synthesis of the formulation in order to produce a variant of DOX® avoiding the formation of DOX_c.

TCSPC: Time Correlated Single Photon Counting; is a technique of acquisition that measure the fluorescence lifetime of a sample by determining the time between the excitation of the sample by a laser pulse and the detection of the emitted photon.

CFD: constant fraction discriminator is an electronic device that generates digital exact time stamps for input signals having changing amplitudes but a constant rise time

TAC: Time to amplitude converter uses an analog technique to convert small time intervals to pulse amplitudes. The device generates an output signal with an amplitude proportional to the time interval between input “start” and “stop” pulses.

DSPE: distearoyl-phosphatidylethanolamine. One of three main lipid components of DOX®.

PEG: Polietilenglicole, is a polymer prepared by polymerization of ethylene oxide.

AFM: Atomic force microscopy is a very-high-resolution type of scanning probe microscopy (SPM), with demonstrated resolution more than 1000 times better than the optical diffraction limit.

EMA: European Medicines Agency: is the Competent Authorities in the evaluation and supervision of medicines, for the benefit of public and animal health in the European Union (EU).

SAXS: Small Angle X-ray Scattering; is a technique by which nanoscale density differences in a sample can be quantified.

DNA: Deoxyribonucleic acid; is the molecule that carries genetic information for the development and functioning of an organism.

RNA: Ribonucleic acid is a polymeric molecule essential in various biological roles in coding, decoding, regulation and expression of genes.

RES: reticuloendothelial system; is a heterogeneous population of phagocytic cells in systemically fixed tissues that play an important role in the clearance of particles and soluble substances in the circulation and tissues, and forms part of the immune system.

CuAAC: Copper-catalyzed Azide-Alkyne Cycloaddition.

GO-DOX: Graphene Oxide Doxorubicin; Nano-vector based on GO nano-sheets.

FDA: Food and Drug Administration; is a federal agency of the Department of Health and Human Services. Is responsible for protecting and promoting public health through the control and supervision of food safety, tobacco products, dietary supplements, prescription and over-the-counter pharmaceutical drugs, vaccines, biopharmaceuticals, blood transfusions, medical devices, electromagnetic radiation emitting devices (ERED), cosmetics, animal foods & feed.

HSPC: phospholipid hydrogenated soy phosphatidylcholine. One of three main lipid components of DOX®.

EPR: enhanced permeability and retention effect; molecules of certain sizes (typically liposomes, nanoparticles, and macromolecular drugs) tend to accumulate in tumor tissue much more than they do in normal tissues.

ADME: absorption, distribution, metabolism and excretion. Describes the disposition of a pharmaceutical compound within an organism. The four criteria all influence the drug levels and kinetics of drug exposure to the tissues and hence influence the performance and pharmacological activity of the compound as a drug.

AIDS: acquired immune deficiency syndrome; is a spectrum of conditions caused by infection with the human immunodeficiency virus (HIV).

Lm^{at}: attenuated *Listeria monocytogenes*; attenuated strain of *Listeria monocytogenes* used for medical research porpoises.

TRAIL: TNF-related apoptosis-inducing ligand; is a protein functioning as a ligand that induces the process of cell death called apoptosis.

BC: biomolecular corona; is the term for the shell of biomolecules (including proteins, lipids, enzymes, etc.) that wrap nanocarriers.

MP: mouse plasma

HP: human plasma

DRs: Death Receptors; is a cell surface receptor of the TNF-receptor superfamily that binds TRAIL and mediates apoptosis.

TNF-receptor: tumor necrosis factor receptor; is a protein superfamily of cytokine receptors characterized by the ability to bind tumor necrosis factors (TNFs) via an extracellular cysteine-rich domain.

Cryo-TEM: Cryogenic Transmission Electron Microscopy; is a cryomicroscopy technique applied on samples cooled to cryogenic temperatures.

AlkDA: alkine-modified D-alanine; probe for the labelling the fifth D-alanine of the peptidoglycan.

AlkDADA: alkyne-D-alanine-D-alanine; probe for the labelling thefourth D-alanine of the peptidoglycan.

Foreword

Cancer is one of the most challenging global healthcare problems. In spite of the large library of drugs available, the goal to selectively kill cancer cells while reducing collateral toxicity to healthy cells remains unsatisfactory. There are several biological barriers to effective drug delivery in cancer such as renal, hepatic, or immune clearance. Nanoparticles loaded with drugs can be designed to overcome these biological barriers to improve efficacy while reducing morbidity. Nanomedicine entered a new era for drug delivery by improving the therapeutic indices of the active pharmaceutical ingredients engineered within nanoparticles. Few of the first-generation nanomedicines have received widespread clinical approval over the past two decades. Among these, Doxil® represents a milestone in the field, being the first FDA-approved nano-drug (1995). It is a uni-lamellar liposome formulation of Doxorubicin (hereafter referred to as 'DOX'). At present, it is used for the treatment of a number of pathologies such as AIDS-related Kaposi's sarcoma, recurrent ovarian cancer, metastatic breast cancer and multiple myeloma. The main characteristics of this formulation are: (i) prolonged drug circulation time (with avoidance of the Reticuloendothelial system, RES), (ii) a protective lipid bilayer in the "liquid ordered" phase composed of high-T_m phosphatidylcholine and cholesterol, (iii) stable loading of a high concentration of DOX molecules (2 mg/ml). Even if the performances of Doxil® are superior with respect to the free drug, there is still no FDA- or EMA-approved generic liposomal formulation available. This is due to the limited understanding of Doxil® "synthetic identity" and reflects into the lack

of analytical tools that can address quantitatively the molecular organization of the drug loaded into the liposomal carrier.

To tackle these issues, in my Thesis I exploited DOX intrinsic fluorescence as a source of signal/contrast and Fluorescence Lifetime Imaging Microscopy (FLIM) as a tool with exquisite sensitivity to the nanoscale to reveal the supramolecular organization of the emitter, the drug itself. In particular, the phasor approach to FLIM data was used as a robust, fast and graphical method to extract the information encrypted within lifetime data. In brief, the fluorescence lifetime decay spectra measured in each pixel in the image are mapped onto a "phasor" plot with coordinates the amplitude and phase of the first harmonic of the Fourier transform of the fluorescence lifetime. Thus, pixels with similar lifetime spectra will have similar coordinates in the phasor plot; also, pixels containing a combination of two different lifetimes spectra will be mapped along the line connecting the positions of the two pure spectra, whose fractional contribution can be easily retrieved. As a model system of encapsulated DOX I analyzed Doxoves®, a research-grade product of PEGylated liposomal DOX whose physical characteristics and pharmacokinetics are comparable to those of Doxil®. First, the phasor-FLIM signature of Doxoves® was resolved into the fractional intensity contribution of three species co-existing within the same nanoparticle, each with its peculiar lifetime, namely: crystallized, free DOX, and membrane-associated DOX. Then, a thorough spectroscopic characterization of the three identified species allowed to extract their true molar fractions within the formulation. The same approach was also used to investigate alternative nanovectors, such as DOX adsorbed onto Graphene-oxide nano-sheets, and DOX-decorated Listeria monocytogenes. The proposed approach may assist in monitoring quantitatively the supramolecular organization of DOX (or similar fluorescent molecules) in every step of the manufacturing chain, from drug

production to drug storage. Furthermore, it can be a promising tool for the investigation of the interaction of the selected formulation with living matter.

The outline of the thesis is the following:

Chapter 1 presents a brief review on the history of Doxil®: from the reasons for which it was synthetized to the methodologies that allowed its realization. In addition, the main reason for the lacking of a generic equivalent of Doxil® is described.

Chapter 2 introduces the phasor approach to Fluorescence Lifetime Imaging Microscopy and the rules of the phasor plot.

Chapter 3 represents the core of the experimental part of the Thesis. In brief, the supramolecular organization of DOX within the standard Doxoves® liposomal formulation (hereafter DOX®) is investigated using visible light and phasor approach to fluorescence lifetime imaging (phasor-FLIM). First, the phasor-FLIM signature of DOX® is resolved into the contribution of three co-existing fluorescent species, each with its characteristic mono-exponential lifetime, namely: crystallized DOX (hereafter DOX_c, 0.2 ns), free DOX (hereafter DOX_f, 1.0 ns), and DOX bound to the liposomal membrane (hereafter DOX_b, 4.5 ns).

Chapter 4 reports on the experiments performed to obtain the exact molar fractions of the three DOX species within DOX®. This is achieved by combining phasor-FLIM with quantitative absorption/fluorescence spectroscopy on DOX_c, DOX_f, and DOX_b pure standards. The final picture on DOX® formulation comprises most of the drug in the crystallized form (~98%), with the remaining fractions divided between free (~1.4%) and membrane-bound drug (~0.7%). Finally, phasor-FLIM in the presence of a DOX dynamic quencher allows us to suggest that DOX_f is both encapsulated and non-encapsulated, and that DOX_b is present on both liposome-membrane leaflets.

Chapter 5 presents the state of art for what concerns the knowledge of the interaction of Doxil® with the living matter and a brief discussion of the future developments of the Thesis project.

Appendix A: summarizes the Materials and Methods used for the experimental procedures described in the Thesis.

Appendix B: presents the Patent resulting from the developing the phasor-FLIM approach to the nanoscale organization of encapsulated drugs.

1

From Doxorubicin to Doxil®: lessons learned

1.1 Introducing Doxorubicin

Doxorubicin (DOX, chemical structure in Fig. 1.1), discovered in the 1960 in the Adriatic see[1–3], is a water-soluble, photosensitive chemotherapeutic drug, produced by the bacteria *Streptomyces peucetius var. caesius*[4]. DOX was approved by the FDA in the 1974[5] for the medical treatment of a wide range of solid and metastatic tumors. This drug has multiple targets at the cellular level and it can induce cell death at low concentration[6] . The cellular uptake of DOX occurs mainly through rapid and passive diffusion, with a detectable effect by either temperature and pH[7]. The intracellular drug accumulates within the nucleus (i.e. it contains about the 80% of the internalized DOX)[8].

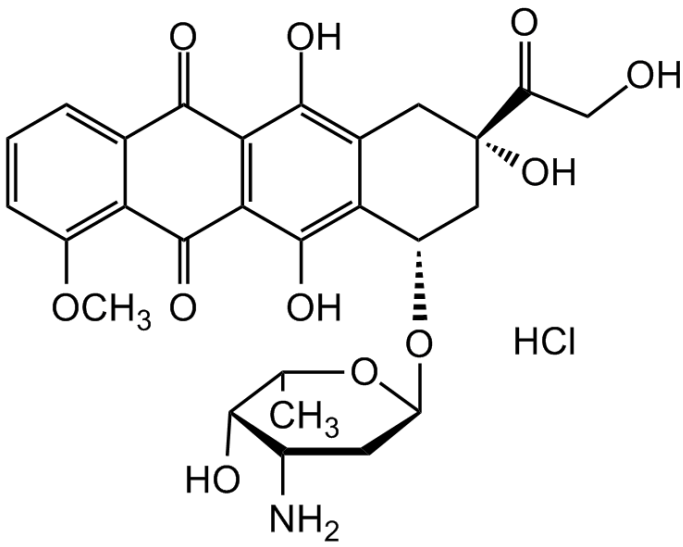

Fig. 1.1 ***DOX****: chemical structure*.

DOX acts on the nucleic acids of dividing cells with two main mechanisms of action. Firstly, it inhibits the DNA and RNA synthesis by intercalating between the base pairs of the double strands of the DNA (Fig. 1.2), preventing the

replication and the transcription of the neoplastic cells. The positively charged mannose amine of the DOX binds efficiently to the negatively charged nucleic acid phosphate diester groups and the anthraquinone planar ring of the drugs shows good affinity for the intercalation into the double-stranded DNA. Secondly, DOX inhibits the enzyme topoisomerase II preventing the relaxation of the supercoiled DNA, and this leads in turn to the block of transcription and replication of DNA. As mentioned above, DOX has multiple targets inside the cells, and can lead to cell death with different mechanisms, primarily apoptosis and necrosis. For example, another biological effect of the drug is that it is able to form iron-mediated free radicals, in turn causing oxidative damages to proteins and membrane lipids.

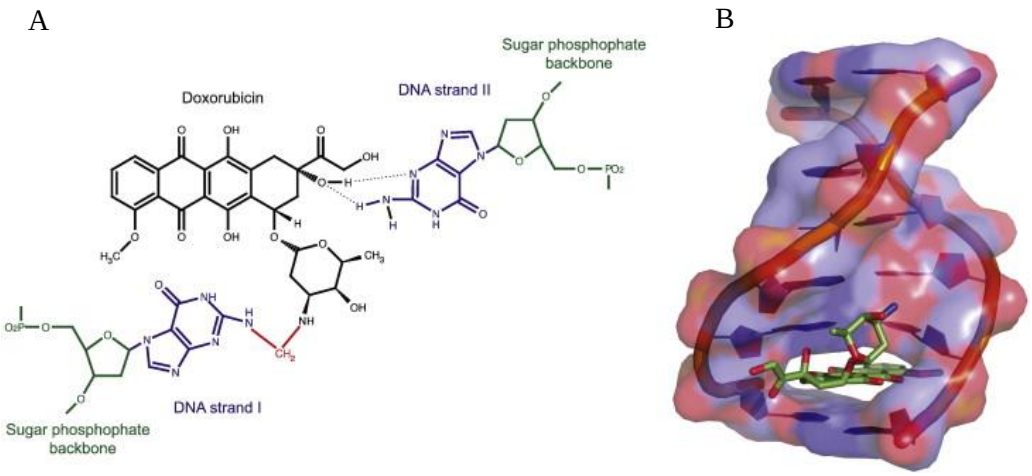

Fig. 1.2 ***Structure of the Doxorubicin-DNA complex:*** *DOX forms a hydrogen bond (dashed line) with guanine on one strand of DNA (DNA strand II) and a covalent bond (displayed in red) with guanine mediated by formaldehyde on the opposing strand (DNA strandII)*[9].

The mitochondrial membranes are particularly sensitive to this effect due the high level of the negatively-charged phospholipid diphosphatidylglycerol (i.e.

cardiolipin, to which DOX has a preferential affinity) in their membranes, [10–13]. The damage induced by oxidative stress is considered one of the main reasons of DOX toxicity[14–16]. Indeed, one of the most severe side effects of DOX is exerted at the level of the heart muscle, deeply enriched in mitochondria, where DOX shows cumulative and dose-dependent cardiotoxicity, with effects ranging from structural or functional changes in myocardial cells to severe cardiomyopathy and congestive heart failure [14–19]. The exact molecular mechanism of DOX-induced cardiotoxicity remains however unclear, making it difficult to predict severe adverse events in patients[20–22]. Several studies have reported that DOX can induce the expression of the Death Receptors (DRs), including TNF receptor 1 (TNFR1), Fas, DR4 and DR5 in several type of cancer, and thereby enhancing TNF-related apoptosis-inducing ligand (TRAIL) induced apoptosis and FAS-mediated apoptosis[23–29]. Interestingly, DR-mediated apoptosis is a very well-conserved pathway in human cardiomyocytes[30–32]. Other common side effects associated to DOX treatment are acute nausea and vomiting, stomatitis, gastrointestinal disturbances, alopecia baldness, neurologic disturbances (hallucinations, vertigo, dizziness), and bonemarrow aplasia, severe myelosuppression (principally granulocytopenia), neutropenia, thrombocytopenia and anemia[33–37]. The combination of DOX clinical use for a broad spectrum of tumor and its defect of dose limiting toxicity made it a very appealing candidate drug for the delivery by nano-carrier. Moreover, the chemical and physicochemical properties of the drug, i.e. its stability and ADME (absorption, distribution, metabolism and excretion) are well established [38–40], as well as its spectral properties (absorption and fluorescence), which allows the quantification of the DOX level, degradation and its aggregation state.

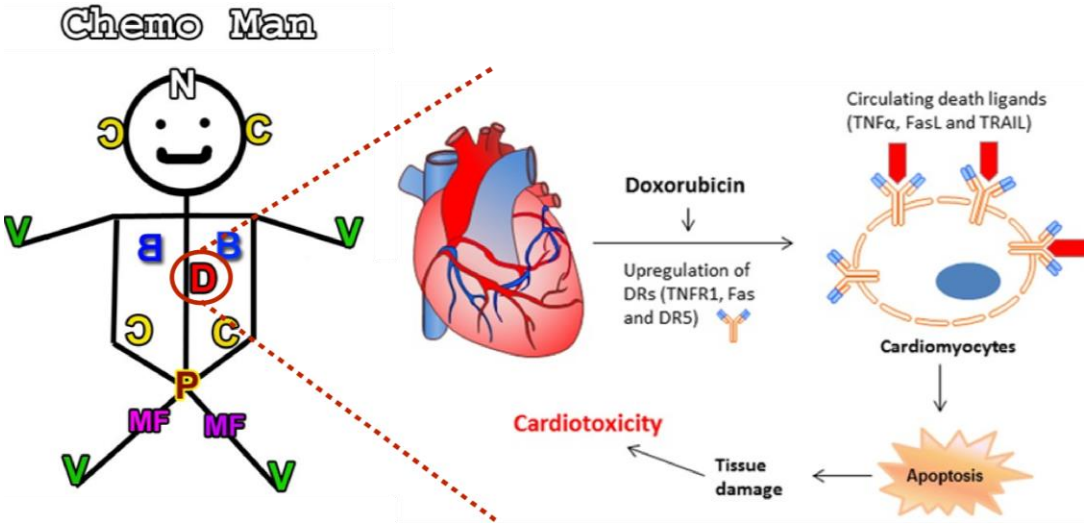

Fig. 1.3 ***Chemo Man:*** *DOX and related anthracyclines appear to be potent inducers of the expression of death receptors (TNFR1, Fas, DR4 and DR5) in cardiomyocytes. The upregulated DRs may undergo clustering or engage their ligands, thereby triggering a caspase cascade and ultimate apoptosis in cardiomyocytes. The elevated serum levels of specific TNF cytokines (e.g., TRAIL), which could occur under certain disease and treatment conditions, may be predictive of the risk of cardiotoxicity in individual patients prior to the administration of doxorubicin or anthracycline agents*[41].

1.2 Doxil®: the first FDA-approved nano-drug

The use of liposomes as drug carriers for chemotherapeutic agents, proposed originally by Gregoriadis in 1981[42], offers a potential means of manipulating drug distribution to improve antitumoral efficacy and reduce toxicity. This idea inspired Barenholtz and Gabizon to rationally engineer what became the first FDA-approved nano-drug in 1995[43]: Doxil® (a schematic history of the major steps in Doxil®development are reported in Fig. 1.4). Doxil®[44] is a liquid suspension of uni-lamellar liposomes of uniform size (around 80-90 nm). The formulation is composed of three main lipid components: HSPC (phospholipid hydrogenated soy phosphatidylcholine), Cholesterol and DSPE (distearoyl-

phosphatidylethanolamine) conjugated with PEG (Polyethylene glycol) in a ratio of 56:38:5 [44,45].

1979	Gabizon and Barenholz started their basic research on liposomal doxorubicin
1984	First clinical trials with liposomal doxorubicin (OLV-DOX which differs to a large extent from Doxil)
1985	LTI licensed the OLV-DOX technology and Barenholz and Gabizon 1990, 1991 I.P. on OLV-DOX
1987	Clinical trial of OLV-DOX failed
1988	Barenholz developed and Yissum, R&D Company of the Hebrew University of Jerusalem, Israel patented new concept of doxorubicin remote loading, the basis of Doxil (Barenholz and Haran 1993, 1994); patents were licensed to LTI
1989	LTI patented the Stealth concept and registered Stealth®
1989	Gabizon and LTI start to develop sterically stabilized (Stealth) liposomes
1989	LTI, Gabizon, and Barenholz start Doxil® development
1991–1992	Doxil "First in man" (FIM) clinical trial in Jerusalem
1994	Gabizon and Barenholz first major publication on Doxil clinical trials (*Cancer Research 1994*)
1995	(November 17) Oncologic Drugs Advisory Committee (ODAC) recommended FDA approval of Doxil
1996	First Doxil sales in USA and Europe
2010	(March) US patent expired

Fig. 1.4 ***Milestones of Doxil®:*** *Timeline of the development of Doxil® from the beginning of research to the expiring of the intellectual protection in US.*

The authors addressed several challenges to develop this nano-formulation and to obtain the FDA approval for the medical use. For instance, since the nanoparticles were designed primarily for the treatment of metastatic tumors, the intravenous administration was the only option. As a consequence, the liposome had to reflect some fundamental characteristics, among which:

i) A characteristic size allowing to extravasate through the structural defects eventually present in the newly-formed blood vessels around the tumor.
ii) Good stability in the bloodstream and good resistance to clearance.
iii) High concentration of the drug within the liposome to reduce the number of injections needed to obtain the desired therapeutic effect.

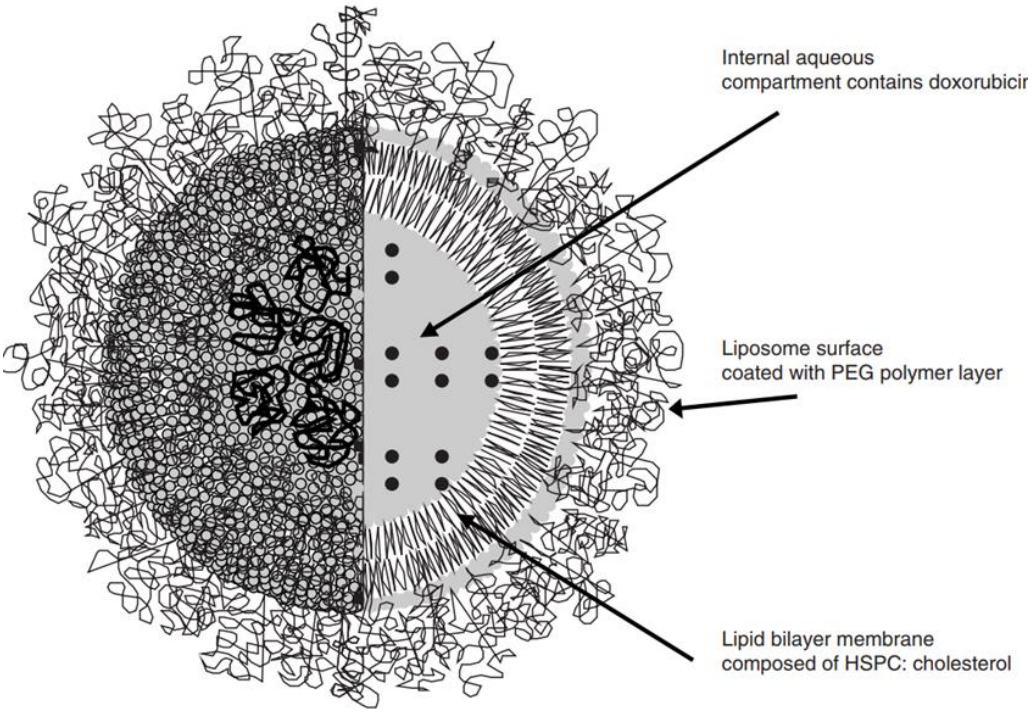

Fig. 1.5 ***First schematic model of the cross-sectional view of Doxil®:*** *A single lipid bilayer membrane separates an internal aqueous compartment from the external medium. DOX is encapsulated in the internal compartment. Polymer groups (linear 2000Da segments) of polyethylene glycol (PEG) are engrafted onto the liposome surface and form a protective hydrophilic layer providing stability to the vesicle. The mean diameter of the liposome is approximately 85nm*[46].

To tackle point (*i*), nano-liposomes with a characteristic size of about 100 nm proved to be superior as compared to the isolated drug in achieving preferential

accumulation at the tumor site, a controversial effect also known as enhanced permeability and retention (EPR) effect. The EPR effect, first described by Matsumura and Maeda[47] and reviewed by Maeda et al.[48] accounts for the selective accumulation of nano-particluates in tumors due to tumor (but not normal healthy tissue) being rich in porous blood capillaries that are permeable to particles of 100 nm and smaller. In addition, the tumor tissue is poor in lymphatic drainage, which enables prolonged retention of the nanoparticles there, followed by local (tumor) drug release and/or for the liposomes to be taken up by the tumor cells.

To tackle point (*ii*) and increase the circulation time of the encapsulated drug, nanoparticles were functionalized with PEG[1]. The suggested mechanism by which PEGylation "works" is that it is a result of the alterations it produces in the physicochemical properties of the molecule to which the PEG residues are covalently attached. These may include changes in level of hydration, conformation, electrostatic binding, and hydrophobicity/hydrophilicity balance. Increasing the level of hydration of the covalently attached PEG (3 to 4 molecules of water per 1 ethylene oxide oxygen) induces changes in structure and leads to increase in the PEG moiety's volume and bulkiness. Altogether, this results in "steric stabilization" which reduces nonspecific protein–protein interaction and nonspecific protein–cell interaction. These physical and chemical changes increase systemic retention of the therapeutic agent. Also, they can influence the binding affinity of the therapeutic moiety to the cell receptors and can alter the absorption and distribution patterns. The highly hydrated groups of this polymer, in fact, act as a barrier by sterically inhibiting the electrostatic and hydrophobic interaction between the surface of the liposomes and different blood components, including opsonins (see schematic representation of opsonin adsorption and PEG effect on the process in Fig. 1.7).

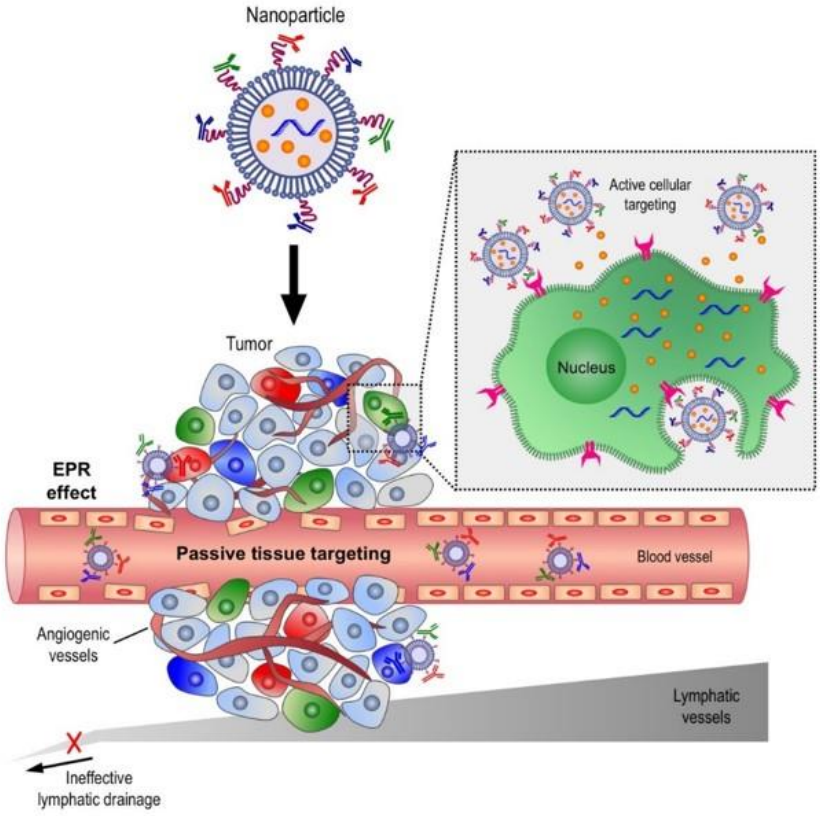

Fig. 1.6 ***Schematic representation of the EPR effect:*** *molecules of certain sizes (typically liposomes or other nanoparticles) tend to accumulate in tumor tissue more than they do in normal tissues. The general explanation that is given for this phenomenon is that, in order for tumor cells to grow quickly, they must stimulate the production of blood vessels. These newly formed tumor vessels are usually abnormal in form and architecture. They are poorly aligned defective endothelial cells with wide fenestrations, lacking a smooth muscle layer or innervation. The nanoparticles, administrated intravenously, are able to extravasate from the wide pores of the newly formed blood vessel in the tumor area*[49].

The functionalization with PEG favors the accumulation of the drug at the tumor site, since nanoparticles with a longer circulation time can perform extravasation more easily through the large fenestrations of the newly formed vessels in the tumor proximity (EPR effect described above, see Fig. 1.6). The liposomes with prolonged circulation time are also named "Stealth®" liposomes.

Finally, to address point (*iii*) and achieve high/stable loading of the drug and reduce the number of needed intravenous injections, new active-loading technologies were introduced.

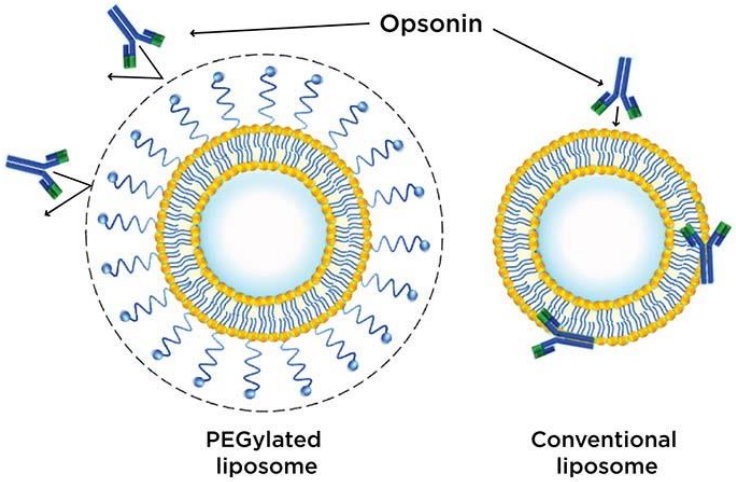

Fig. 1.7 ***Schematic comparison of PEGylated liposome with the conventional one:*** *PEGylated liposome: higher molecular size, good solubility, and shielded against opsonin. Conventional liposome: small molecular size, poor solubility, and it is not shielded against blood component (e.g. opsonin)* [50].

By standard passive-loading methodologies, in fact, the therapeutic concentration of the drug could not be easily reached and, at the same time, very large amounts of lipids were administered. The first study demonstrating the active remote-loading of an amphipathic weak-base molecule was carried out by Deamer and co-workers[51,52] (see Fig. 1.8). In this approach, liposomes are prepared in a solution of ammonium sulfate at the desired concentration.

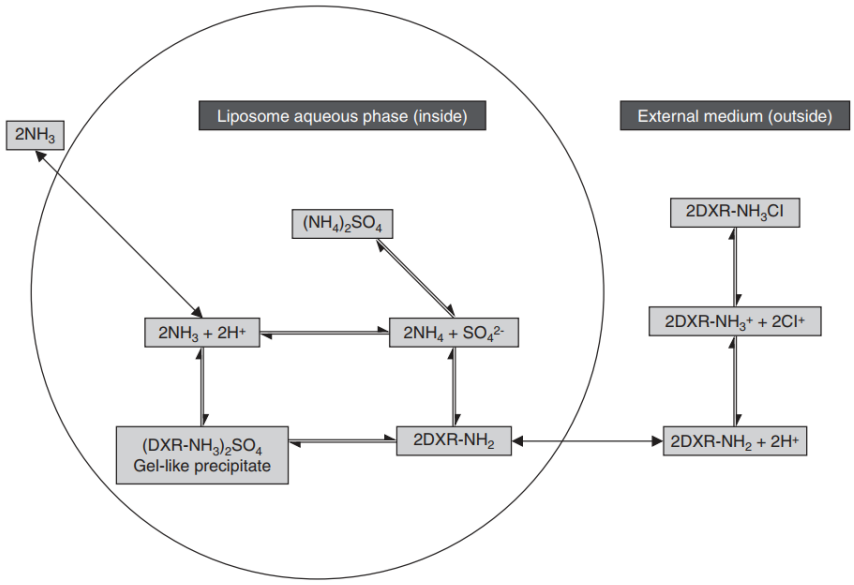

Fig. 1.8 ***DOX remote loading****: Ammonium sulfate gradient driven loading of doxorubicin into the intraliposomal aqueous phase. Liposomes are prepared at the desired concentration of ammonium sulfate. The gradient [$(NH_4)_2SO_4$]lip≫[$(NH_4)_2SO_4$]med »1000 was formed by removing the ammonium sulfate from the external liposome medium either by dialysis or gel filtration. Intraliposomal NH_4^+ dissociates into NH_3 , which easily escapes from the liposome, and H+ ions which are retained in the liposomal water phase. DOX HCl is added to the liposome dispersion at a temperature above the phase transition of the liposomal lipids. DOX, is in equilibrium between an ionized form and a non-ionized form. The latter form shuttles across the liposome bilayer, becomes ionized once exposed to the internal environment rich in proton, and forms a salt with the SO_4^{2-} anions. This leads to gradual liposome entrapment of doxorubicin with high efficiency (>95%) and within short incubation times (~1 hour)* [46].

A specific concentration gradient between the internal and external media, with [$(NH_4)_2SO_4$]lip ≫ [$(NH_4)_2SO_4$]med ("lip" is the aqueous core of the liposome, "med" is the external medium), is then reached by removing the ammonium sulfate from the external medium by dialysis or gel filtration. Inside the liposome the NH_4^+ separates into NH_3 (that can escape from the liposome) and H^+ (that remains in the aqueous core). The temperature of the dispersion is raised above the phase transition temperature of the liposomal lipids and DOX-HCl is added. DOX gets into equilibrium between an ionized and a non-ionized form; this last

one form shuttles across the membrane and, once exposed to the proton-rich core environment, becomes ionized and forms a salt with SO_4^{2-} anions. This finally enables entrapment of DOX with an efficiency higher than 95%.

1.3 The actual synthetic identity of Doxil®

As mentioned in the previous paragraph, the rationale behind the production of Doxil® was that of obtaining a rather simple unilamellar liposome functionalized with PEG and containing DOX at very high concentration (as represented in Fig. 1.5). Thanks to the use of semi-quantitative high-resolution techniques, such as Cryo-TEM, however, a more complete understanding of the actual synthetic identity of Doxil® after drug active loading was achieved. As shown in Fig 1.9 (panel 'B'), the presence of a nanorod crystal-like structure was unveiled in the liposomal core. This structure is formed during the process of the active remote loading. Indeed, the salt resulting from the interaction of the ionized DOX and SO_4^{2-}anions is insoluble and tends to precipitate and aggregate forming crystal-like nanorod-shaped structures[53–56]. The presence of this structure was also confirmed by SAXS measurements[56]. It is now well-documented that the formation of this crystal-like nanorod of precipitated DOX depends strictly on the intraliposomal concentration of ammonium sulfate used during the remote loading process[57]. In fact, only if the ammonium sulfate concentration is above a certain threshold (i.e. higher than approximately 150 mM) nanorods will form (Fig. 1.9, upper panel). Below the same threshold, incomplete or even no formation of the crystal-like structure will be observed (Fig. 1.9A, bottom panel, and Fig. 1.9C, TEM micrograph).

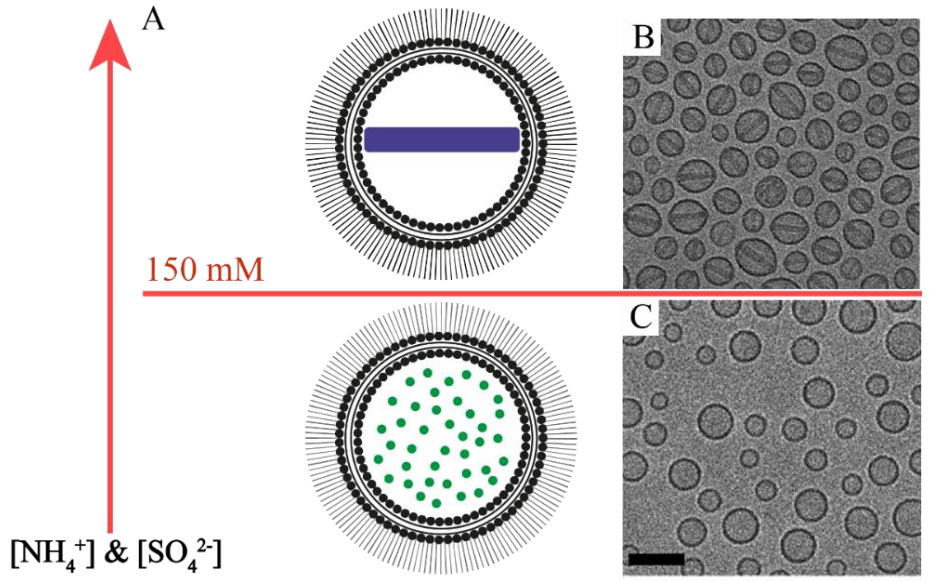

Fig. 1.9 ***Crystal-like nanorods formation****: A) schematic representation of the concentration "threshold" of [NH_4^+] and [SO_4^{2-}] needed for the formation of the nanorod crystal structure of DOX*[57]*. B) cryo-TEM of a Doxil® synthetized with a concentration above the threshold. C) cryo-TEM of a Doxil® synthetized with a concentration below the threshold* [45]

In addition, the loading efficiency at an ammonium-sulfate concentration higher than 150 mM can reach values above 95%. Instead, the liposomes prepared at an ammonium sulfate concentration below 150 mM typically yield loading efficiencies below 90%.

1.4 Doxil® efficacy in pre-clinical and clinical studies

Several preclinical and clinical trials for Doxil® were carried out in the last 30 years. In preclinical studies, Doxil® showed a long circulation time in plasma, an higher accumulation at the tumor site in several animal models, together with a superior therapeutic activity as compared to the standard therapy, i.e free DOX. Then, in the first clinical trial on human subjects (1991-1994[58]) Doxil®

demonstrated higher tumor accumulation with respect the free drug, used as control of standard care. These data represent a first evidence, in a human model, of passive accumulation at the tumor by the EPR effect[58]. In fact, this study demonstrates higher levels of the drug in tumor cells and tumor interstitial fluids after Doxil® administration as compared to the same experiment performed with the isolated drug (Fig. 1.10).

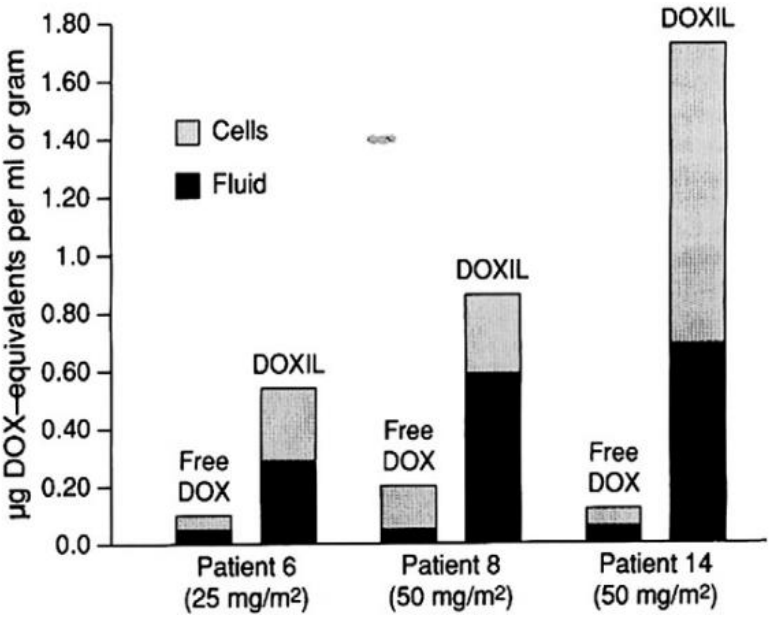

Fig.1.10 ***clinical trial with Human subject****: DOX levels in tumor biopsies of human patients, comparing Doxil® and free DOX*[59]*. As it is possible to see with the same concentration of drug administered there is a much higher accumulation in the biopsy samples of patients treated with Doxil®. The data are the first proof for the EPR effect induced in tumors by passive targeting in humans. The accumulation of Doxil® in human tumors was further supported by direct fluorescence microscopy on patient biopsies.*

Clinical studies conducted on human subjects revealed that, overall, Doxil® improves patient daily compliance. Of particular note, cardiotoxicity gets markedly reduced as compared to the standard care, which in turn allows

increasing the overall treatment duration. The details of the Doxil® clinical performance are a topic covered extensively in many publications.

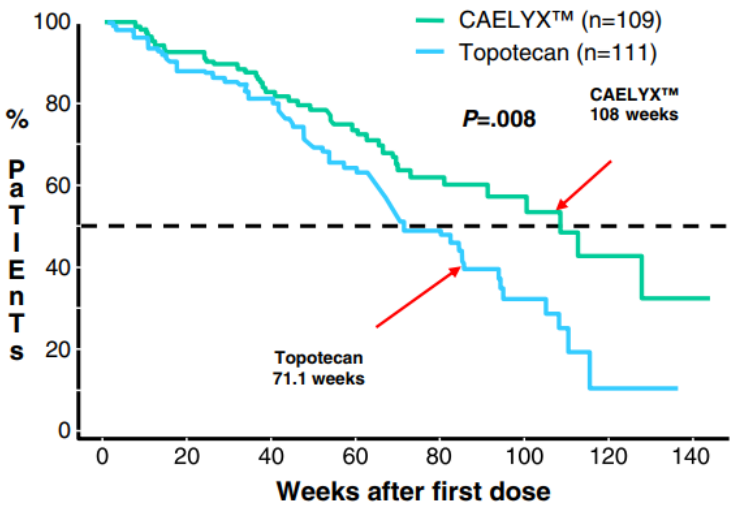

Fig.1.11 ***Doxil® performances****: Clinical trial to compare the efficacy of treatment with Doxil® (= CAELYX) with respect to treatment with topotecan in ovarian cancer patients*[45]*. As it is possible to see there was a significant difference in overall survival favoring pegylated liposomal doxorubicin, with medians of 108 versus 71.1 weeks (P =.008).*

In brief, the target tumors for which the use of Doxil® was approved by the U.S. Food and Drug Administration (FDA) and by the European Medicines Evaluation Agency (EMA) agencies include:

- AIDS-related Kaposi's sarcoma: superior efficacy compared to standard-of-care therapy.
- Metastatic breast cancer: equivalent efficacy and lower cardiotoxicity compared to free DOX.
- Recurrent ovarian cancer: superior efficacy and enhanced safety profile of Doxil® as compared to the isolated drug, based on available studies[60] (Fig. 1.11).

- Multiple myeloma: equivalent efficacy and improved safety profile compared to free drugs.

1.5 Lessons learned and motivation for this Thesis work

The patent protection of Doxil® in the USA is over since 2010, but no generic PEGylated liposomal DOX analog was approved by FDA or EMA so far. Possible explanations for the lack of a generic liposomal DOX are thoroughly discussed in a review by Jiang and collaborators from the Office of Generic Drugs at the FDA[61]. Citing verbatim:

"The explanation for the lack of generic Doxil is that such a generic product ***is much more difficult to develop than a simple drug****, or even than biologicals such as antibodies, because in addition to what is needed for the approval of generic low molecular weight drugs and biologicals, for approval of generic liposomal drugs, there are additional physical and physicochemical requirements needed. An example?* ***Deciphering the state of the encapsulated drug"***

(W. Jiang, FDA Officer)

W. Jiang, R. Lionberger, L.X. Yu, In vitro and in vivo characterizations of PEGylated liposomal DOX, Bioanalysis 3 (2015) 333–344.

As clearly pointed out by these words, the understanding of the in-cuvette "synthetic identity" of this DOX liposomal formulation, i.e. the set of physicochemical properties resulting from production, has a key role in development of a generic Doxil® or in the research for new drug formulations. Limitations largely stem from the lack of analytical tools that can quantitatively

dissect the molecular organization of the drug within the intact liposomal formulation. To date, high-resolution techniques (e.g. cryo-EM, SAXS) can provide only a semi-quantitative analysis of such formulations, typically not sufficient, for instance, to distinguish possible coexisting phase-separated drug pools within the same formulation and eventually quantify their fractional amount. These limitations affect our ability to control the performance of encapsulated DOX in delivery applications, and to improve by rational design their efficacy. Based on what said, it may appear clear that a fast analytical procedure capable to characterize the supramolecular organization of an encapsulated drug, Doxorubicin in the case-study selected here, would represent a significant step forward in the field. In this regard, it is interestingly to note that many FDA-approved molecules are characterized, in terms of chemical structure, by the presence of aromatic rings, a structural feature that makes them very similar to natural fluorophores (se exemplary cases reported in Fig. 1.12). In this regard, DOX is not an exception: indeed, the spectral characteristics of DOX are well documented in the scientific literature[45]. The chemical structure of DOX is made up of a tetrahydroxy-anthraquinone, a duanosamine sugar with a hanging glycosyl moiety, essentially representing the structure of anthracycline antibiotics[62–64]. For this reason, DOX shows an intrinsic fluorescence which can be exploited as a valuable tool in research and imaging[65–68]. In fact, the photophysical properties of DOX (Fig. 2.13 A,B) in aqueous solution have been the object of a large number of studies including UV-vis absorption, NMR and fluorescence spectroscopy[69–76]. Also the fluorescence lifetime of the drug was already investigated and characterized: it was reported that DOX in aqueous solution displays a mono-exponential or bi-exponential lifetime decay depending on the aggregation state of the drug [73,75,76,79–81].

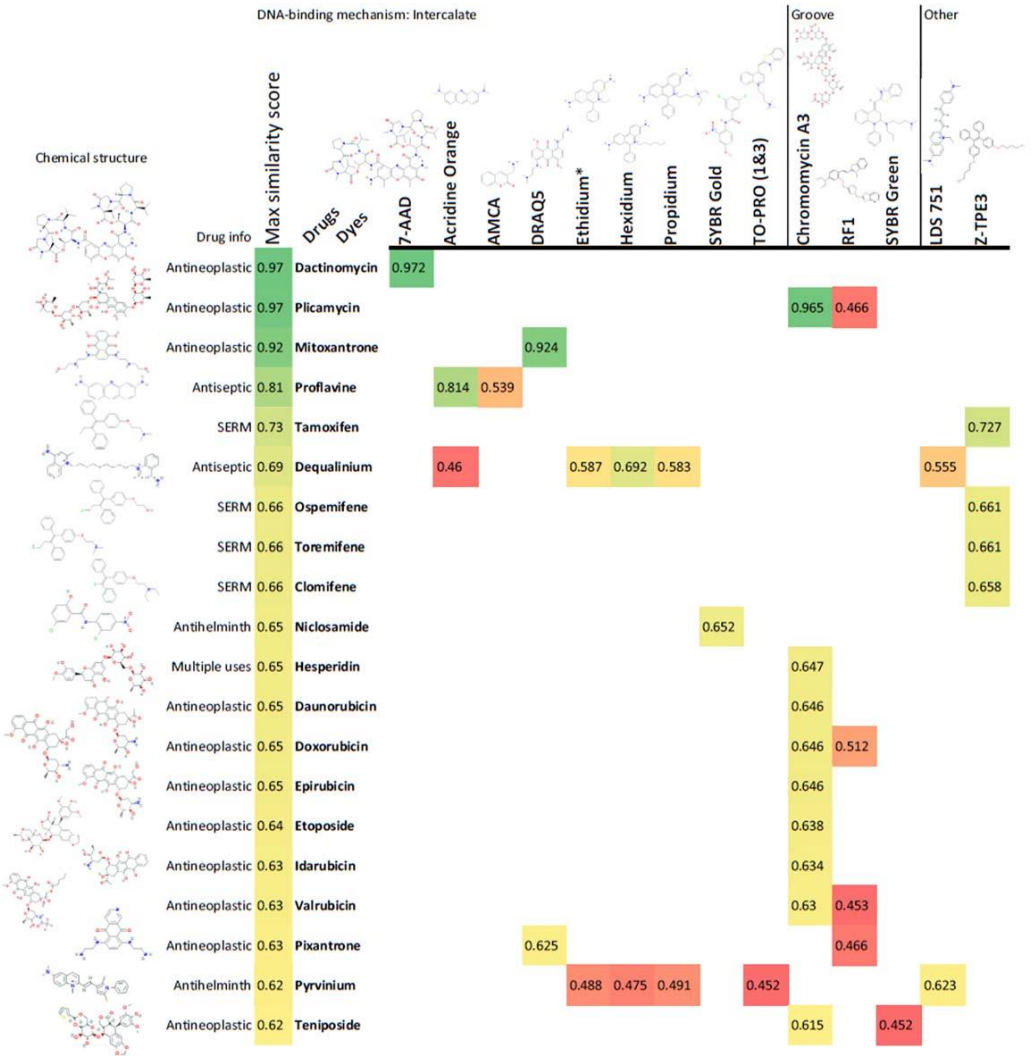

Fig. 1.12 ***Top 20 FDA-approved drugs with structural similarity to non-approved fluorescent dyes:*** *Drugs are organized based on the higher similarity score to research dye(s) with the color representing a low to a high similarity from red to yellow to green; * indicates classic semi-impermeable cell stain for comparison*[77].

In particular, the non-aggregated form yields mono-exponential decay with characteristic time of about 1.0 nanosecond (Fig. 1.13C). Furthermore, the intensity of DOX fluorescence significantly decreases after the intercalation into the DNA: the fluorescence quantum yield is 30–40 times lower compared to the non-intercalated drug[71,82].

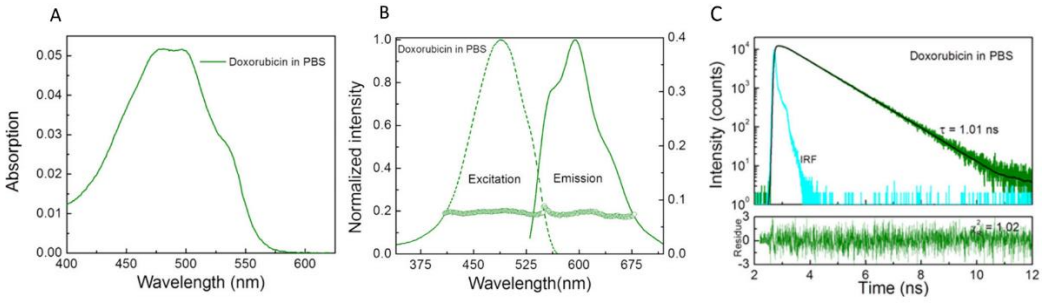

Fig. 1.13 ***DOX spectra****: A) Absorption spectra of Doxorubicin in PBS buffer. B) Excitation and fluorescence spectra of Doxorubicin in PBS buffer; The fluorescence excitation spectra were measured at 600 nm and fluorescence emission spectra were excited at 500 nm*[78]*. C) Fluorescence lifetime of Doxorubicin in PBS buffer*[78]*.*

Also, DOX has a higher quantum yield if embedded into an hydrophobic environment, for instance within lipidic structures such as membranes and/or after binding to macromolecules[83]. Building on this knowledge, we decided to exploit DOX intrinsic fluorescence as a source of signal/contrast and fluorescence lifetime imaging microscopy (FLIM) as a tool with exquisite sensitivity to the nanoscale supramolecular organization of the emitter.

2

Fluorescence Lifetime Imaging Microscopy

2.1 Fluorescence Lifetime

A fluorophore which is excited by a photon will drop to the ground state with a certain probability based on the decay rates through a number of different (radiative and/or nonradiative) decay pathways. To observe fluorescence, one of these pathways must be by spontaneous emission of a photon. In the ensemble description, the fluorescence emitted will decay with time according to

$$I(t) = I_0 e^{-t/\tau} \qquad Eq.2.1$$

where

$$\frac{1}{\tau} = \sum k_i \qquad Eq.2.2$$

In the above, t is time, τ is the fluorescence lifetime, I_0 is the initial fluorescence at t=0, and k_i are the rates for each decay pathway, at least one of which must be the fluorescence decay rate k_f. More importantly, the lifetime, τ is independent of the initial intensity and of the emitted light. This can be utilized for making non-intensity based measurements in chemical sensing. Fluorescence-lifetime imaging microscopy or FLIM is an imaging technique based on the differences in the exponential decay rate of the photon emission of a fluorophore from a sample. It can be used as an imaging technique in confocal microscopy, two-photon excitation microscopy, and multiphoton tomography. The fluorescence lifetime of the fluorophore, rather than its intensity, is used to create the image in FLIM. Fluorescence lifetime depends on the local micro-environment of the fluorophore, thus precluding any erroneous measurements in fluorescence intensity due to change in brightness of the light source, background light intensity or limited photo-bleaching. This technique also has the advantage of minimizing the effect of photon scattering in thick layers of sample. Being

dependent on the micro-environment, lifetime measurements have been used as an indicator for pH, viscosity and chemical species concentration.

2.2 Time Correlated Single Photon Counting (TCSPC)

At present most of the measurements of fluorescence lifetimes are performed in the time domain by using a pulsed source and time-correlated single-photon counting (TCSPC). The principle of TCSPC is somewhat unique. The sample is excited with a pulse of light. For TCSPC the conditions are adjusted so that less than one photon is detected per laser pulse. In fact, the detection rate is typically 1 photon per 100 excitation pulses. The time is measured between the excitation pulse and the observed photon and stored in a histogram. The x-axis is the time difference and the y-axis the number of photons detected for this time difference. When much less than 1 photon is detected per excitation pulse, the histogram represents the waveform of the decay. If the count rate is higher the histogram is biased to shorter times. This is because with TCSPC only the first photon can be observed. At present the electronics are not fast enough to measure multiple photons per pulse when the lifetimes are in the nanosecond range. Multiple photons per pulse can be measured for decay times near a microsecond or longer. Specialized electronics are used for measuring the time delay between the excitation and emission. The experiment starts with the excitation pulse that excites the samples and sends a signal to the electronics. This signal is passed through a constant fraction discriminator (CFD), which accurately measures the arrival time of the pulse. This signal is passed to a time-to-amplitude converter (TAC), which generates a voltage ramp that is a voltage that increases linearly with time on the nanosecond timescale. A second channel detects the pulse from the single detected photon. The arrival time of the signal is accurately determined using a CFD, which sends a signal to stop the voltage ramp. The TAC now

contains a voltage proportional to the time delay between the excitation and emission signals. The voltage is converted to a digital value that is stored as a single event with the measured time delay. A histogram of the decay is measured by repeating this process numerous times with a pulsed-light source. Present electronics for TCSPC only allow detection of the first arriving photon.

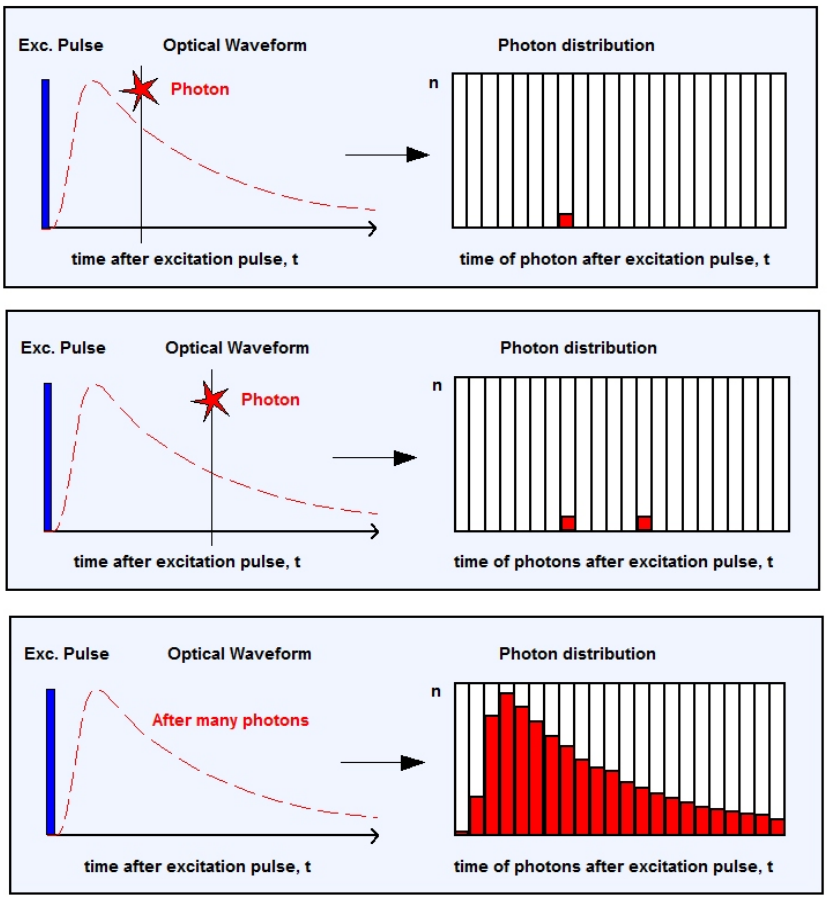

Fig. 2.1 ***TCSPC****: Schematic representation of the measurement of start-stop times in TCSPC. TCSPC detects the times of the photons arrival after the excitation pulses. The photon detection rate is much lower than the pulse repetition rate of the signal. Consequently, the detection of several photons per signal period is extremely improbable. Under these conditions, the time of this photon can be determined at extremely high resolution. From the times of the individual photons TCSPC builds up the distribution of the photons over the time after the excitation pulse*[84].

The dead times range from 10 microseconds in older systems to about 120 ns with modern TCSPC electronics. These times are much longer than the fluorescence decay. The dead time in the electronics prevents detection of another photon resulting from the same excitation pulse. Recall that emission is a random event. Following the excitation pulse, more photons are emitted at early times than at late times. If all these photons could be measured, then the histogram of arrival times would represent the intensity decay. However, if many arrive, and only the first is counted, then the intensity decay is distorted to shorter times.

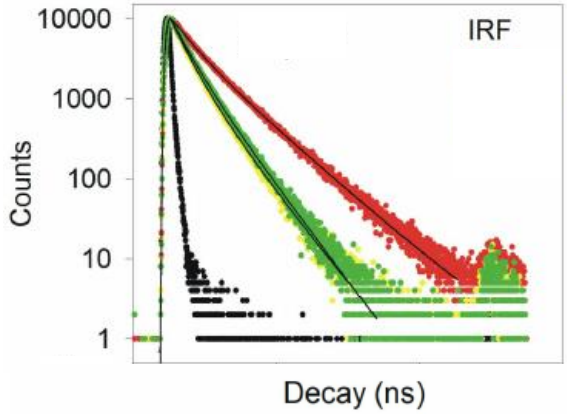

Fig. 2.2 ***Fluorescence Lifetime:*** *Decay curve of two different fluorophores. The fluorophore represented by the red decay curve has a longer fluorescent lifetime with respect to the one represented by the green decay curve.*

2.3 Phasor Analysis

If we have a decay curve represented by an exponential function (Eq. 2.3) the Fourier Transform at the angular repetition frequency ω of the laser pulse will result in a complex number composed by a real and an imaginary component (Eq. 2.4). This complex number can be graphically represented in a 2D plot where the

imaginary part becomes the Y axis (also named ‘s’ component) and the real part becomes the X axis (also named ‘g’ component).

$$d(t) = d^{0e^{-t/\tau}} \qquad \text{Eq. 2.3}$$

$$D(\omega) = \frac{1}{1+j\omega\tau} = \frac{1}{1+j\omega\tau}\frac{1-j\omega\tau}{1-j\omega\tau} = \frac{1-j\omega\tau}{1+(\omega\tau)^2}$$

$$= \frac{1}{1+(\omega\tau)^2} - j\frac{\omega\tau}{1+(\omega\tau)^2} \qquad \text{Eq. 2.4}$$

Mapping the imaginary versus the real part of the function highlights a semicircle (also named ‘universal semicircle’ Fig. 2.3) whose semi-circumference corresponds to purely mono-exponential lifetimes (from Eq. 2.4 it is easy to see that the lifetime equal to ‘zero’ nanoseconds is located at the coordinate (1,0), lifetime equal to infinite is located at (0,0)).

All possible combinations of mono-exponential lifetimes (i.e. multi-exponential decays) will corresponds to point in the phasor plot located within the semicircle. By this analysis, in summary, each decay is transformed into a unique position on the phasor plot which depends on its average lifetime. The most important feature of this analysis is that it is fast and it provides a graphical representation of the measured curve. The actual lifetime value can be always retrieved by calculating the magnitude of the phasor through Eq. 2.5:

$$\tau = \frac{1}{\omega}\frac{Im\,D(\omega)}{Re\,D(\omega)} \qquad \text{Eq. 2.5}$$

In a non-ideal and real situation, the measured decay curve is the convolution of the instrument response (the laser pulse distorted by system) with an exponential function which makes the analysis more complicated.

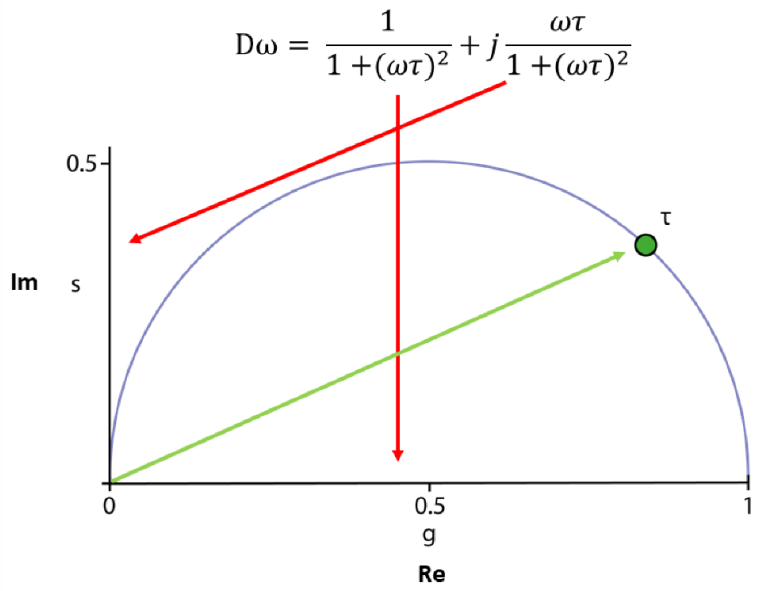

Fig. 2.3 ***Phasor Plot****: Schematic illustration of the phasor plot. The blue semi-circles represent the universal circle, centered in 0.5. The green circle represents a cluster of phasors of a fluorescent pure species having a monoexponential decay to the ground state. The coordinates s and g are respectively the imaginary and the real part of the Fourier transform.*

Large number of techniques have been developed to overcome to this problem but in phasor approach this is simply solved by the fact that the Fourier transformation of a convolution is the product of Fourier transforms. This allows to take into account the effect of instrument response by taking the Fourier transformation of instrument response function and dividing the total phasor to instrument response transformation.

2.4 Phasor composition rules

As stated above, the semi-circumference represents all possible single exponential fluorescent decays. When the measured decay curve consists of a superposition of different mono-exponential decays, the phasor falls inside the

semicircle depending on the fractional contributions of the components. For example, if two different fluorescent species are measured in the same pixel, the resulting phasors will be distributed along the line connecting the characteristic phasors of the two pure species (Fig. 2.4, left panel). Furthermore, if we have an experimental phasor that is the combination of two (or more) fluorescent species, and if we know the positions of the phasors of the isolated species, it is also possible to calculate the fractional intensity of the contribution of the pure species.

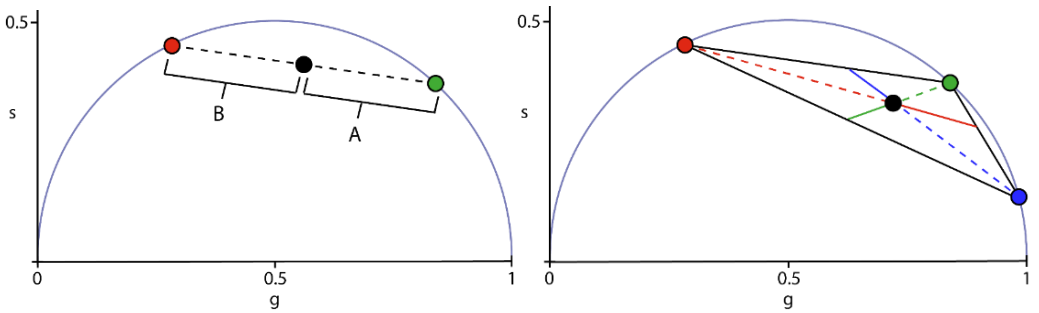

Fig. 2.4 ***Phasor composition rules****: Left panel: Schematic illustration of a phasor plot of complex sample resulting of a mixture of two different fluorophores having two different lifetimes. The red and green dots are the pure species, the black dot represents the complex sample under investigation, lying on the conjunction line (dashed line) of the two pure species. Right panel: Schematic illustration of the phasor plot resulting from the measurement of a complex species of three different fluorophores. The red, green and blue dots represent the single pure species, and they are the vertex of the drown triangle. The black dot represents the complex sample under investigation. The (red, green and blue) dashed lines represent the conjunction line between the phasors of the sample and the vertex of the triangle (pure species), the colored continuous lines (the lines from the black dot to the black line of the triangle) are used to calculate the fractional intensity of the different component.*

So, if we have a bi-exponential decay the overall intensity decay can be written as:

$$I(t) = A_b e^{-t/\tau_b} + A_c e^{-t/\tau_c} \qquad \text{Eq. 2.6}$$

where :

- A_b and A_c are the amplitude of the exponential components
- τ_b and τ_c are the lifetime of the two species

The phasor coordinates ('g' and 's'), according to Eq. 2.4 will be:

$$g(\omega) = \left(A_b\tau_b \frac{1}{1+(\omega\tau_b)^2} + A_c\tau_c \frac{1}{1+(\omega\tau_c)^2}\right) / (A_b\tau_b + A_c\tau_c) \qquad \text{Eq. 2.7}$$

$$s(\omega) = \left(A_b\tau_b \frac{\omega\tau_b}{1+(\omega\tau_b)^2} + A_c\tau_c \frac{\omega\tau_c}{1+(\omega\tau_c)^2}\right) / (A_b\tau_b + A_c\tau_c) \qquad \text{Eq. 2.8}$$

where ω is the angular repetition frequency of the laser. These equations can be simplified with the use of the fractional intensity (F) of each species "n", according to the definition:

$$F_n = A_n\tau_n / \sum_n A_n\tau_n \qquad \text{Eq. 2.9}$$

So rewriting the coordinates of the phasors, we obtain:

$$g(\omega) = \left(F_b \frac{1}{1+(\omega\tau_b)^2} + F_c \frac{1}{1+(\omega\tau_c)^2}\right) \qquad \text{Eq. 2.10}$$

$$s(\omega) = \left(F_b \frac{\omega\tau_b}{1+(\omega\tau_b)^2} + F_c \frac{\omega\tau_c}{1+(\omega\tau_c)^2}\right) \qquad \text{Eq. 2.11}$$

With: $F_b + F_c = 1$

The final equation is the law of phasor addition for a two-species model, but it can be applied to any number of species. In the case of a sample with three different fluorescent molecules, for instance, it is possible to draw a triangle whose vertices are the characteristic phasors of the three pure species (Fig. 2.4, right panel). Then, a line connecting the phasors of the pure species and the phasor of the composite sample can be drawn and then extended to the opposite side of the triangle (see dashed segments in Fig. 2.4, right panel). These segments

can be used for the calculation of the fractional intensity contribution of each pure species "i" using the following relation:

$$Fi = \frac{distance_{point \rightarrow intercept}}{distance_{i \rightarrow intercept}} \qquad \text{Eq. 2.12}$$

where '*point'* represents the experimental position of the phasors of the composite sample. The phasor approach is growing as a tool for FLIM analysis due the possibility to obtain a fast and quantitative result in a visually straightforward manner without the need of high concentration of fluorophores[85–87].

2.5 Phasor-FLIM analysis of Doxorubicin in aqueous solution

To start with a benchmark measurement, we measured the phasor-FLIM signature of DOX in a water solution. As stated in chapter 1.5, the fluorescence-lifetime properties of DOX dissolved in a aqueous solution is expected to be nearly mono-exponential with a characteristic decay time of about 1.0 nanosecond[88,89]. As already quoted in Appendix A ("Materials and Methods" section), the calibration of the setup for the acquisition was performed by measuring the known mono-exponential fluorescence decay of Fluorescein at pH equal to 11, which has a purely mono-exponential lifetime of 4.0 ns. As expected, and reported in Fig. 2.5B, DOX in aqueous solution yields a mono-exponential decay lying on the universal semi-circumference of the phasor plot at the expected position of ~1.0 nanosecond.

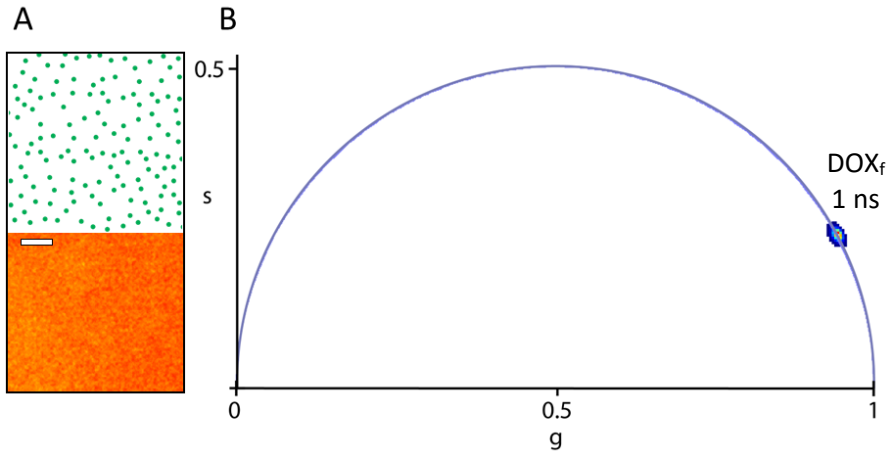

Fig. 2.5 ***Experimental phasor of DOX in aqueous solution****: A) upper panel: schematic representation of the solution of DOX in water. Lower panel: experimental FLIM image of the solution of DOX in water, scale bar 5 μm. B) Phasor Plot of experimental FLIM acquisition of DOX solution in water.*

3

Phasor-FLIM analysis of the supramolecular organization of liposomal Doxorubicin

3.1 Phasor-FLIM analysis of liposomal Doxorubicin

As model of PEGylated liposomal-encapsulated DOX we analyzed Doxoves® (hereafter: DOX®), whose physical and chemical characteristics are comparable with those of original Doxil®. The datasheet of the product indicates that DOX® formulation comes with more than 98% of the drug molecules encapsulated within the liposomes, presumably all in the form of a nanorod-shaped crystal (hereafter: DOX_c), while the remaining fraction of the drugs are supposed to be in a free form in the solution, presumably not encapsulated (hereafter: DOX_f). We started our investigation by analyzing the lifetime of DOX®. DOX® yields the characteristics of a multi-exponential decay, as it is possible to see in Fig 3.1. Since we have already seen that the phasors cluster of DOX_f in aqueous solution fall along the universal circle, showing a mono-exponential decay of ~ 1.0 ns, we shall assume that different conformations of DOX contribute to DOX® average lifetime. So, to have a complete model of the organization of DOX inside the liposome it is necessary to perform a FLIM measurement of the DOX_c as a pure species, since is the only other conformation that is known to be present inside the liposomes. The DOX-sulfate nanorods crystal-like structure was synthesized following the protocols of Wei et al.[90]: adding dropwise an aqueous solution of DOX to a solution of ammonium sulfate under a vigorous magnetic stirring until the formation of insoluble precipitate, then it was dry-out un a WillCo plate (for further information see Materials and Methods in Appendix A). DOX_c are characterized by phasors cluster on a spot along the universal center, so once again a mono-exponential decay, corresponding to a lifetime of ~ 0.2 ns. The result from FLIM measurement of DOX_f and DOX_c are highly reproducible (SD<1%). As can be seen in Fig. 3.2C, a trajectory (black solid line) along which all the possible mixtures of DOX_f and DOX_c species are expected to lie can be easily identified.

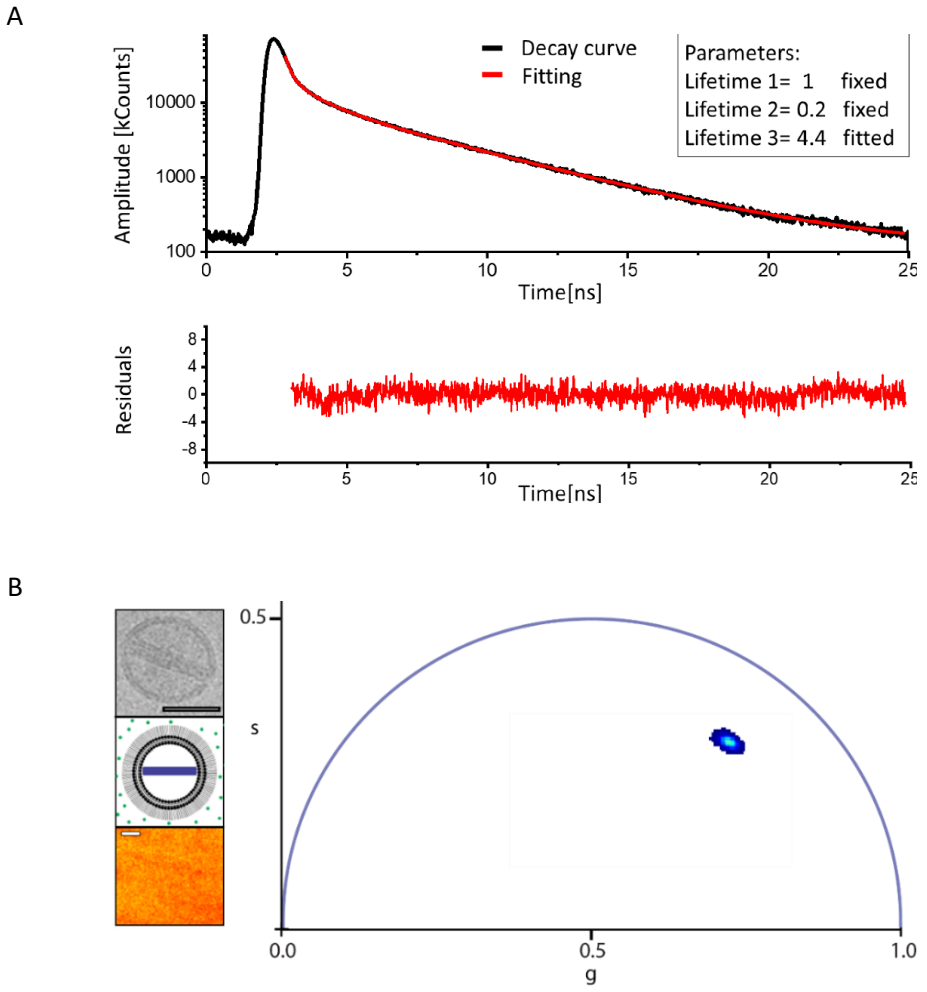

Fig. 3.1 ***DOX®lifetime decay and phasor transformation****: A) Upper panel: data fitting in the time domain suggests that the hypothetical third species should be characterized by a lifetime higher than ~4 ns. Top panel: typical lifetime decay curve of DOX® (black) with multiexponential fitting with three components (red). Bottom panel: fitting residues. B) Left panel, respectively from the top to the bottom: Cryo-TEM of DOX® (scale bar 50 nm)*[91]*, a schematic representation of DOX® and the FLIM measurement of DOX® (scale bar 5μm). Right panel: Phasor plot of the FLIM measurement of DOX®.*

Quite surprisingly, however, the measured phasor-FLIM signature of DOX® does not lie on the expected segment. In order to rationalize the experimental DOX®

lifetime, at least one third species must be present in the mixture. In order to find this hypothetical third species, a simplified system in which DOX_c species was selectively removed from the formulation was synthetized.

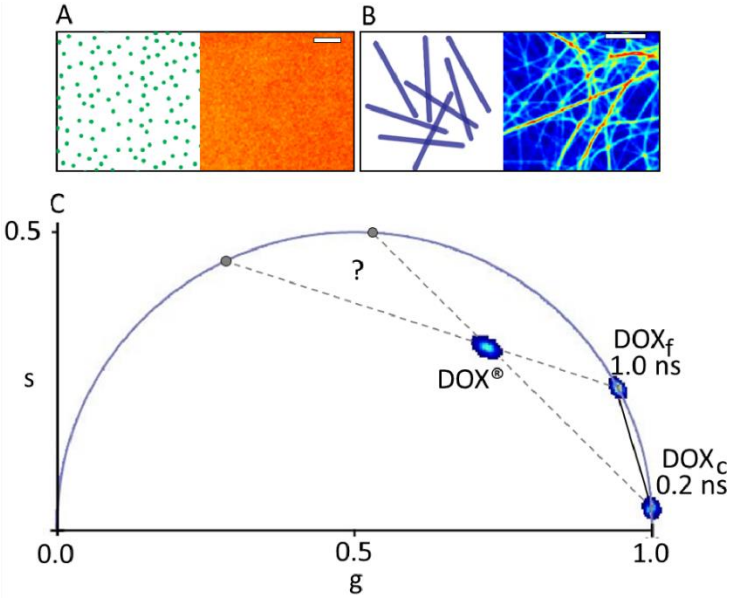

Fig.3.2 ***Phasor-FLIM fingerprint of DOX®****: A-B) Schematic drawing of DOX_f in aqueous solution, isolated DOX_c, in solution, respectively (left panels) with the corresponding confocal FLIM images (right panels). Scale bars: 5 µm. C) Phasor plot containing the lifetime data from the three samples described above: DOX_f (cluster of phasors on the universal circle at ~1 ns), DOX_c (cluster of phasors on the universal circle at ~0.2 ns), and DOX® (cluster within the universal circle). The grey dashed lines indicate a possible area for a third species.*

In particular, we exploited the protocol by Wei and collaborators in which, by using a low concentration of ammonium sulfate during drug loading, precipitation of the drug is avoided and a new formulation without DOX_c is obtained (hereafter DOX®-like nanoparticles or DLN). The multi-exponential nature of the corresponding experimental lifetime (Fig. 3.3 A-B) confirms the presence of at least of a second (unknown) species other than DOX_f in the DLN.

This evidence leads to the hypothesis that the candidate as additional species is represented by the drugs molecules associated/bound to the lipidic membrane of the liposomes.

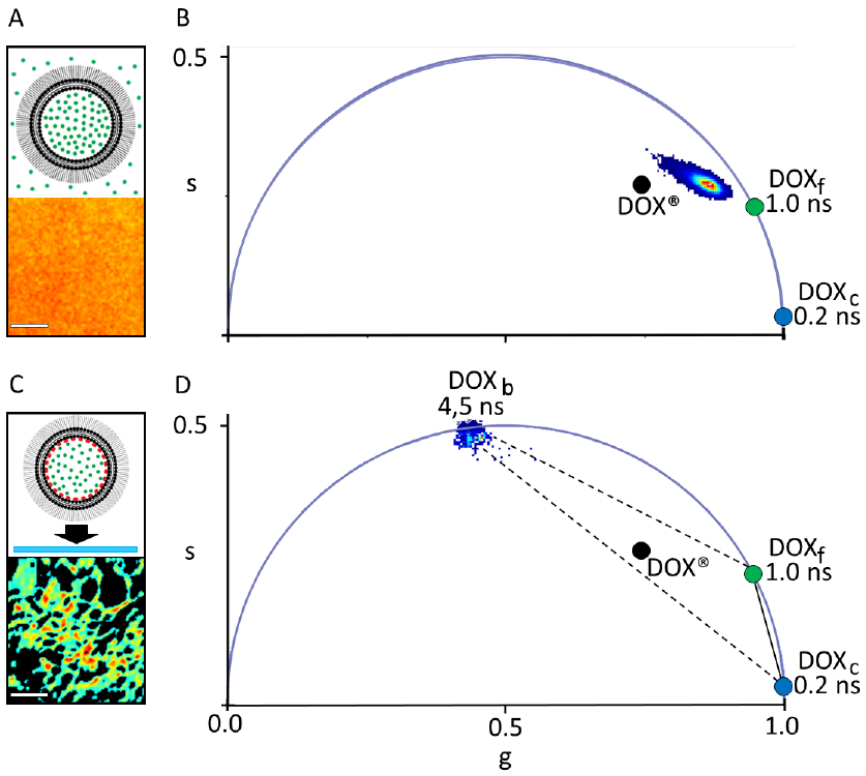

Fig. 3.3 Phasor-FLIM fingerprint of DNL*: A) Schematic representation of the sample (top) and the corresponding confocal image for DLN in solution (bottom). B) Phasor plot containing the clusters measured from DLN in solution. C) Schematic of DLN spin-coated on glass (top) and the corresponding confocal image for DLN spin-coated on glass (Bottom). D) B) Phasor plot containing the clusters measured from DLN after spin-coating. Scale bars: 3 µm. The black dot corresponds to the centroid of the cluster "DOX®" in Fig. 3.1B.*

To test this hypothesis, we used the spin-coater to mechanically destroy the DLN particles on a glass. After washing the sample to eliminate residues of DOX_f we carried out the FLIM measurement. The result phasor-FLIM analysis of these membrane patches (hereafter DOX_b) is nearly mono-exponential with a lifetime

of ~ 4.5 ns (Fig. 3.3C-D) and highly reproducible. These results resemble data from literature obtained from DOX molecules attached via imine bonds to a polymeric surface of iron-oxide nanoparticles[92]. The next step was repeating the spin-coater experiment with DOX® in order to have a confirmation of the data obtained since now. Interestingly, after the spin-coater it was possible to observe patches corresponding to both DOX_c and DOX_b, yielding phasor clusters in two different regions of the phasor plot which are very close to the spot corresponding to lifetime 0.2 ns and 4.5 ns, respectively (Fig. 3.4).

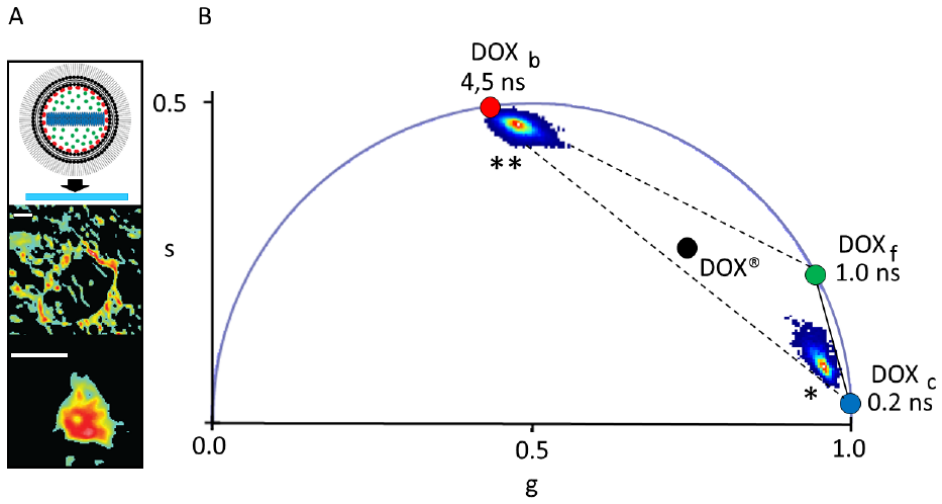

Fig. 3.4 Phasor-FLIM analysis of DOX® synthetic identity*: A) Schematic representation of the sample (top) and the confocal acquisition of DOX_b (middle) and DOX_c (bottom). B) Phasor plot containing the two clusters obtained if DOX® is spin-coated on glass, corresponding to the DOX_b (marked **) and DOX_c (marked *) components of DOX®. The two components were measured separately as DOX_c-enriched patches on the glass were sensibly less fluorescent than DOX_b-enriched patches. Scale bars: 3 µm. The black dot corresponds to the centroid of the cluster "DOX®" in Fig. 3.1B.*

These experiments confirm the hypothesis that DOX_f, DOX_c and DOX_b are present within the intact DOX® nanoparticles. The identification of the third species allows us to determine the fractional intensity contribution of the single

species. It should be noted that the phasor cluster of DOX® represents an average of measurements conducted on multiple liposomes. While it is possible to extract an average of the contributions of the three pure species from these measurements, it cannot be guaranteed that all measured DOX® particles have the same composition of DOX_b, DOX_f, and DOX_c.

3.2 Fractional Intensity contribution

The fractional-intensity contribution of each species can be determined from the position of the DOX® phasor-plot cluster in the triangle with the three pure species as vertices, using algebraic rules (Eq. 2.12 Chapter 2). Obtained results are reported in the pie-chart of Fig. 3.5A and in Tab. 1 (column '$DOX^{®}_{FLIM}$'). Please note that, at this level, the procedure can already be used to quantitatively compare different datasets (e.g. distinct drug preparations; see data from a second batch reported in Fig. 3.5B).

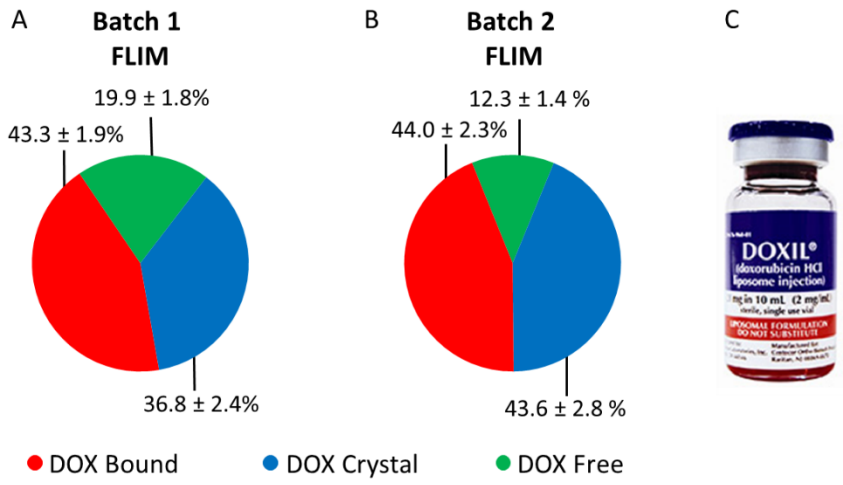

Fig. 3.5 ***Fractional intensities****: A-B) pie-chart representing the fractional-intensity contributions of the three DOX species within two different batch of DOX®. Batch 1 is the one used for the experimental measurements described in this thesis. C) Batch of Doxil® commercial formulation.*

Still, the fractional-intensity contribution of a species will coincide with its actual molar fraction only if the distinct pure species have the same brightness (given by the product of their quantum yield QY and their molar absorption coefficient ε) under the experimental conditions used. This issue will be addressed in the next Chapter.

4

From fractional intensities to molar fractions

4.1 From fractional Intensity contribution to molar fraction

The fractional intensity contribution of each species can coincide with its molar fraction only if pure species have the same brightness (i.e. the product of their molar absorption coefficient, or ε, and their quantum yield, or QY), under the same experimental conditions. To measure the brightness of the different species, the first step was measuring the QY of DOX_f exciting it at 488 using an integration sphere following the protocol of Mello et al. [93]

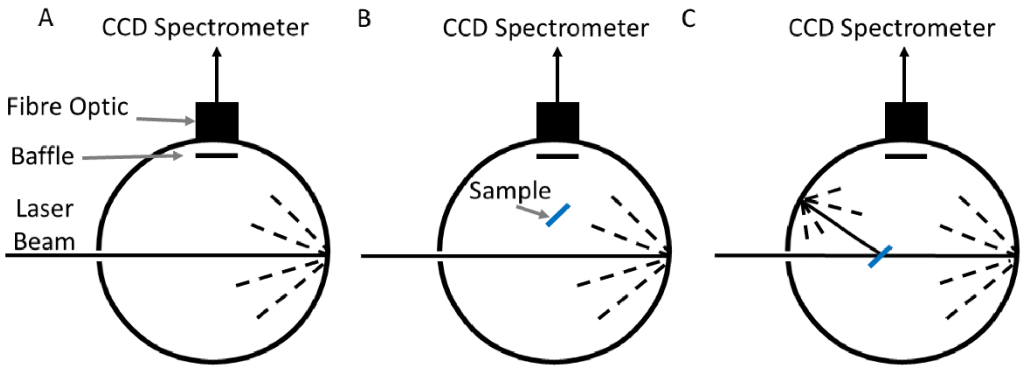

Fig. 4.1 ***Integration sphere setup:*** *Illustration of the three configurations of the sphere. A) the sphere is empty; B) the sample in in place and the laser beam is directed onto the sphere wall; C) the sample is in place and the laser beam is directed onto the sample.*

In brief, a calibrated broadband lamp was used to illuminate the samples [94] and the resulting spectra of optical signals collected by the integration sphere were measured by a fiber-coupled monochromator (mod. Flame, Ocean Optics). The integration sphere was also used for the absorption and the QY of DOX_f and DOX_c[94]. In brief the samples were optically stimulated by a diode laser (mod. L6Cc, Oxxius) at 488 nm, and a diode (LED) with emission peak at 470 nm was used for the evaluation of the absorption. A fiber-coupled monochromator was used to measure the intensity of the excitation laser and of the fluorescence

emitted by the samples. These procedures were executed in different configuration, following the protocols from literature. The obtained QY was ~ 4.2%, value in line with the literature [95]. We exploited the Lambert-Beer relation to derive the molar absorption coefficient of DOX_f at 470 nm (or ε_{470}) by using the measured absorbance, the concentration of the free drugs and the optical path: the result of the calculation is ~10340 $M^{-1}cm^{-1}$, once again a value in good agreement with the literature[96]. We used the measurement on DOX as a calibration for similar quantification of DOX_c sample.

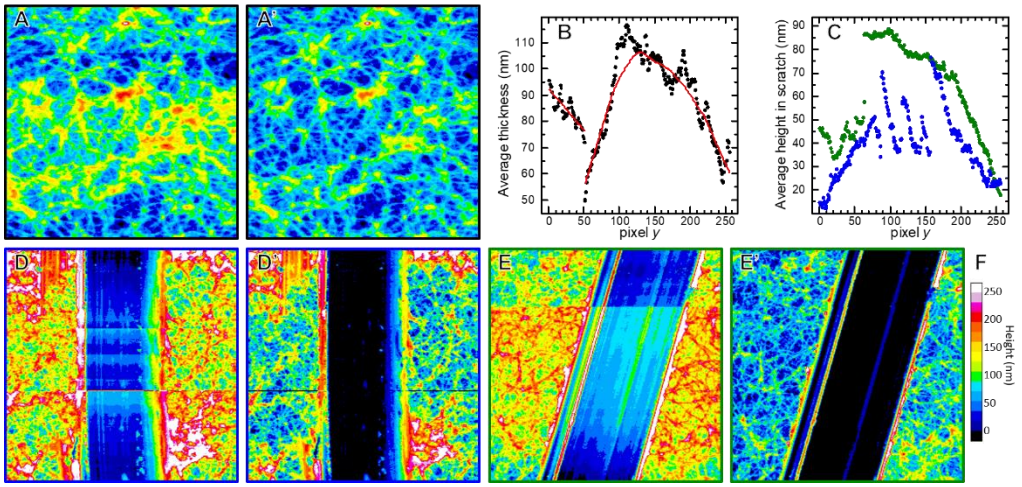

Fig. 4.2 ***Atomic Force Microscopy:*** *AFM images of DOX_c deposited on a glass, and their detrending. A-A') AFM image of the sample before and after applying the correction along y. B) Black dots: average along x as a function of y for the image in panel A. Red curves: smoothing of the data in two different regions, used for correcting the image in A. C) Blue and green dots: average along x (as a function of y) of the heights measured by AFM inside the scratch visible in the AFM images of the scratched sample reported in panels D and E, respectively. These values were subtracted from all the pixels with corresponding y in the figures in panels D and E in order to obtain the images in panels D' and E', respectively. F) Common color scale for the heights represented in the images in panels A, A' and D-E'); all images are of square areas of 40 μm side.*

We found out that the QY of DOX_c at 488 nm was significantly decreased with respect to the free drug, that is: ~ 0.15%. The quantification of the ε_{470} of the crystal was obtained by combining the absorbance (measured by the integration sphere method) with a careful experimental estimate of the effective optical path in the DOX_c sample. The Atomic Force Microscopy was used to measure the optical path of the sample (Fig. 4.2). The AFM acquisitions presented a trend and some discontinuities on heights along the secondary scanned axis (y). Two different strategies were used to detrending. In the first one the sample was scanned as it was and it was calculated the average along x for every row y. Then it was performed a smoothing in every section where no discontinuities were present (Savitzy-Golay with 51 points of windows and polynomial order 3), then the result was subtracted from all the pixels having the same y and it was added a constant in order to obtain the minimum height at 0.

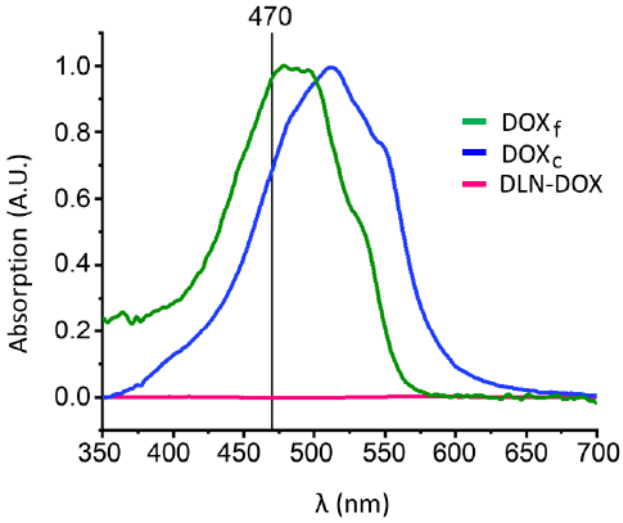

Fig. 4.3 ***Sphere Measurements:*** *Absorption spectra measured with the integration sphere of DOX_f (green line) and DOX_c (blue line). Spectra were normalized to 1 (A.U.). Absorption spectra of DLN and DOX_f (measured as described in Materials and Methods and normalized to 1) displayed almost no differences (magenta line) so they are superimposable.*

In the second strategies carried out on the same samples, it was done a scratch more or less in y direction. From the zones within the scratch, where no residue was present, it was obtained the average measured height at a given y, and this value was subtracted for all the pixel with such y. The value ε_{470} obtained was ~7150 $M^{-1}cm^{-1}$ (see paragraph 4.2).

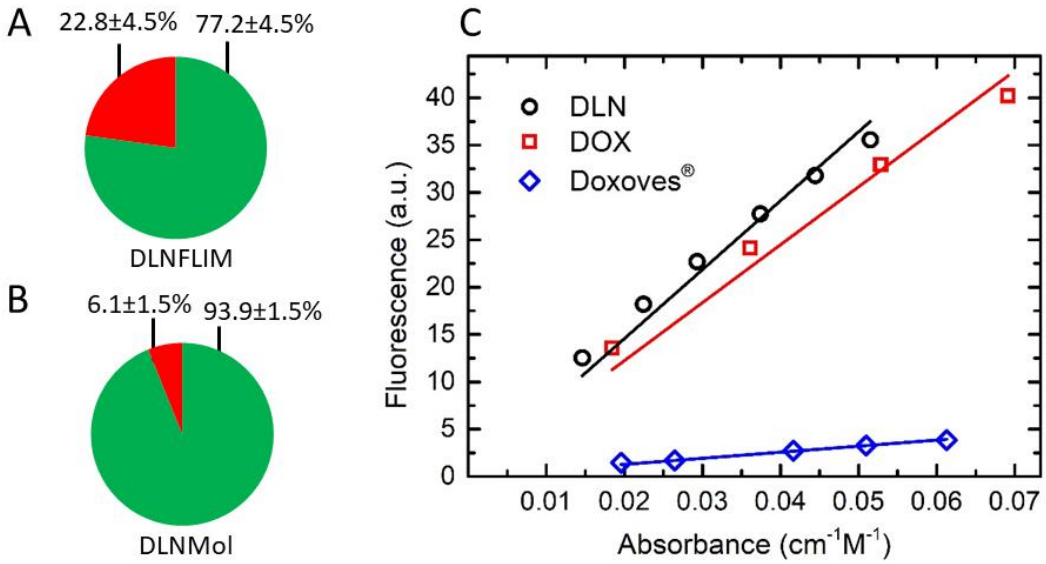

Fig. 4.4 ***Components of DLN:*** *A) Pie chart of the fractional-intensity contribution of DOX_f and DOX_b within the DLN. B) Pie chart of the molar fraction of DOX_f and DOX_b within the DLN. C) Black dots, red squares, and blue diamond shows the area under the peak of fluorescence emission versus absorbance at 470nm (after the remotion of the background, estimated with a linear fit in the ranges 350±10, 580±10) for DLN (black dots), DOX (red squares), and DOX® (blue diamonds) at different concentrations. The black, red and blue lines are the linear fits (with intercept fixed at 0) of DLN, DOX and DOX®, respectively. Ratios between the slopes correspond to ratio between QYs, and DOX was used as reference material. Absolute QYs values were calculated by using the QY value of DOX experimentally detected here (4.23±0.09%). The resulting QYs are 5.03±0.25% for DLN and 0.45±0.02% for DOX®.*

The difference between the ε_{470} values of DOX_c with respect to DOX_f is not completely surprising, especially in light of the red-shift of the absorption spectrum (Fig 4.3) observed measuring the two different samples. For what

concern the membrane-bound drugs we assumed, according with literature[95], that the QYs of DOX_f and DOX_b are in the same ratio of their lifetimes (leading to a QY of 19% for DOX_b) and that the ε_{470} is the same for the two species.

Table 1

	Pure species			**Composite species**			
	DOX_f	**DOX_c**	**DOX_b**	**DLN_{FLIM}**	**DLN_{mol}**	**$DOX^{®}_{FLIM}$**	**$DOX^{®}_{mol}$**
N	12	7	4	7	7	24	24
τ_m (ns)	1.002±0.008	0.200±0.001	4.54±0.04	3.45±0.05	-	2.32±0.06	-
DOX_f (%)	100	-	-	77.2±4.5	93.9±1.5	19.9±1.8	**1.37±0. 22**
DOX_b (%)	-	-	100	22.8±4.5	6.1±1.5	43.3±1.9	**0.66±0.08**
DOX_c (%)	-	100	-	-	-	36.8±2.4	**97.98±0.29**
QY_{488} (%)	4.23±0.09	0.150±0.004	*19.17±0.47*[ʎ]	ND	5.14±0.25[§]	ND	0.40±0.03[§]
ε_{470} ($M^{-1}cm^{-1}$)	10340±35	7510±490	*10340±35*[¥]	ND	-	ND	-

Table 1. Cumulative results extracted from phasor-FLIM and spectroscopic measurements. *In the first column named "pure species" are reported all the measurements conducted on DOC_f, DOX_b and DOX_c. In the second column named "composed species" are reported the fractional intensities and the molar fraction (respectively named as FLIM and Mol) of the pure species included in the DLN and DOX® formulations, after the phasors analysis. All values are expressed as Mean±SD except for QY and ε_{470} which are expressed as Mean±SE. For derivation of the uncertainties, see paragraph 4.2.*

Then, we were able to derive the molar fraction of DOX_b and DOX_f within DLN from the FLIM data and we use them to estimate the value of QY of DLN

(QY_{DLN}=5.14±0.25%, Eq. 4.9, details in paragraph 4.2). To test this estimate we carried out measurements of absorption/fluorescence spectroscopy of DLN in-cuvette to obtain their experimental QY: the value is 5.03 ± 0.25%, in good agreement with our estimate (Fig. 4.3, details in paragraph 4.2). We used these results to convert the fractional intensity contribution of the three conformations of the drug within DOX® into their molar fraction (Fig. 4.5, details in paragraph 4.2, Eq. 4.6). As it is possible to see in Fig. 4.5 and in Table 1, there is a dominance of the DOX_c component (~ 98%), in good agreement with the expectations from the procedure of active-loading of the drug[45,97]. The minor fraction is represented by DOX_b (~0.7%), data that is not present in literature but is not in contrast with reports on the nature of DOX-membrane interaction[98]. Finally, the molar fraction of DOX_f (~1.4%) appears to be in line with the manufacturer's expectations for non-encapsulated DOX (<2%).

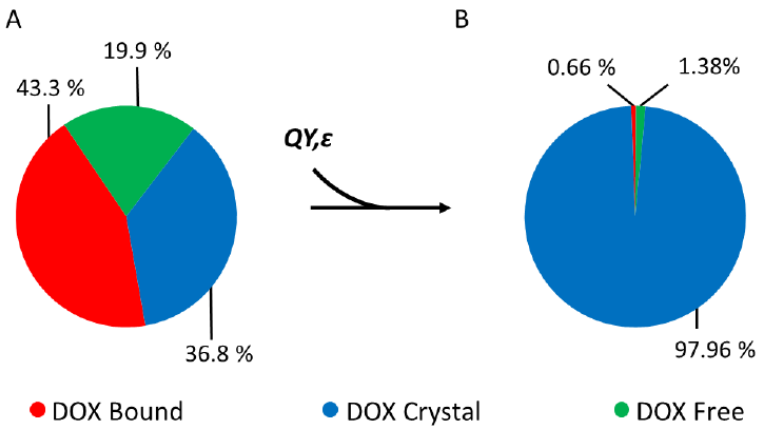

Fig. 4.5 ***Quantification of the molar fractions of the three DOX species within DOX®:*** *Quantification of the molar fractions of the three DOX species within DOX®. A) The fractional-intensity contributions of the three DOX species within DOX® represented by a pie-chart. B) Pie-chart representing the molar fractions of the different species after correction by QY and ε.*

It remains unclear, however, if a fraction of DOX_f is trapped within the aqueous lumen of DOX®. In order to investigate this last point, we carried out FLIM measurements on DOX® before and after incubation with KI (370 mM), a dynamic quencher of non-encapsulated DOX (Fig. 4.6).

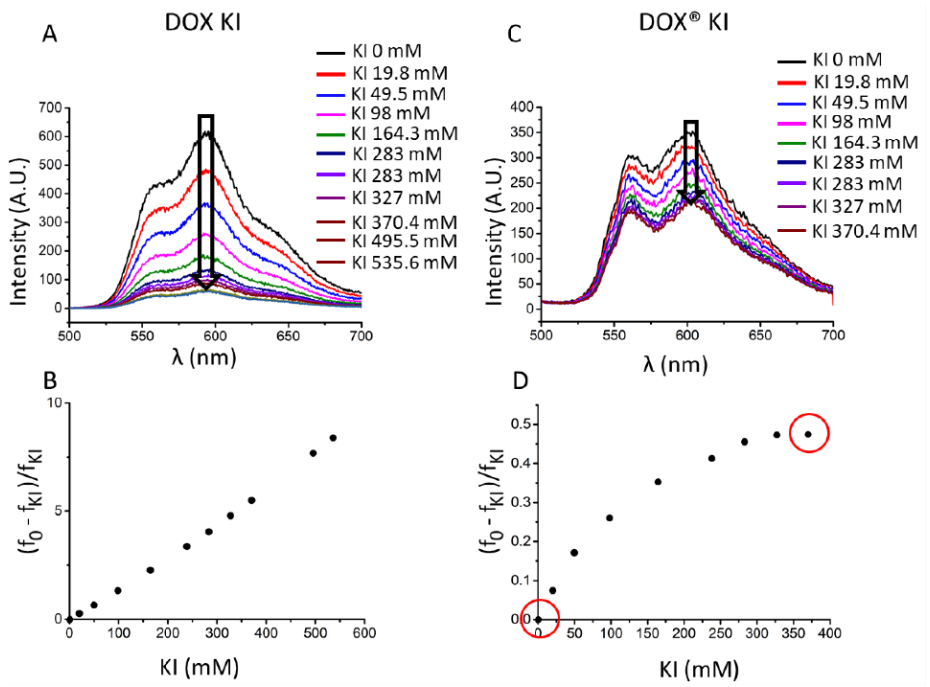

Fig. 4.6 ***KI experiments****: (A) Effect on DOX fluorescence emission (excited at 470 nm) after the administration of KI at different concentrations: KI is an effective quencher of DOX molecules in solution. (B) (f0-fKI)/f0, where f0 (fKI) is the fluorescence intensity at 600 nm excited at 470 nm of a* DOX_f *sample without and with KI, plotted as a function of KI concentration. (C-D) Same experiments as in (A-B), but using DOX® instead of free form of DOX. In this case, KI is able to quench only a fraction of DOX molecules (i.e. in 'D' is possible to see that the plot reaches a plateau at high KI concentrations). The two experimental conditions indicated by the red circles (without KI and 370 mM KI) were measured also by FLIM (Fig 4.6).*

With the assumption that DOX_c cannot be quenched by KI, the lifetime data from our experiment (N=3) suggest that a fraction of the DOX_f is trapped inside the

liposomes (~35%), while the remaining fraction (~65%) is non-encapsulated (Fig.4.7).

A

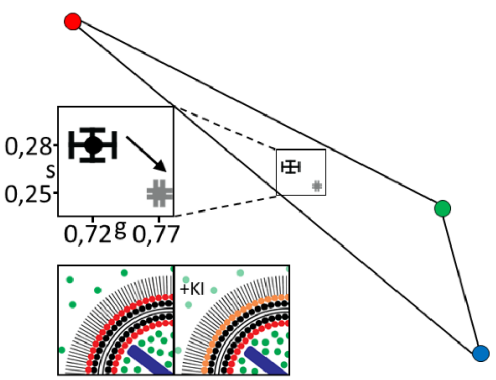

B

	DOX® FLIM (pre-KI) †	DOX® FLIM (post-KI) ‡	DOX® (%Ex/In) ‖	
N	3	3	-	
DOX_f (%)	22.1±1.0	11.2±0.34	Ex%	65.1±4.3
			In%	34.9±4.3
DOX_b (%)	44.4±2.5	40.1±2.5	Ex%	37.9±6.9
			In%	62.1±6.9
DOX_c (%)	33.5±3.4	48.7±2.2	In%	100

Fig. 4.7 ***Quantification of the molar fractions of the free DOX inside and outside of DOX®:*** *A) schematic phasor plot of DOX® before (black) and after (grey) the incubation with KI, corresponding to the two drowning at the bottom of the plot: green dots are DOXf molecules, red dot are representing DOX_b, the corresponding faded colors are the molecules quenched by KI. B) In the second column (†) are present the results from N=3 experiments conducted on DOX® in absence of KI (reported as Mean±SD); in the third column (‡) are displayed the results from N=3 experiments conducted on DOX® in presence of 370 mM KI (reported as Mean±SD); in the fourth column (‖) are displayed the percentages of external ('Ex') and internal ('In') DOXf and DOX_b; the percentage reported here were calculated as described in paragraph 4.2 (Eqs. 10,11) with the assumption that DOX_c, being buried within the core of liposome, is not affected by the membrane-impermeable KI (values are Mean±SD).*

Worthy of note, the data indicate that also a fraction of DOX_b is affected by KI (~38%), suggesting that DOX molecules can interact with both of the layer of the liposomes during the loading of the drugs, but there is a prevalence of molecules on the inner one. Thus, the percentage of drug inside and outside the liposome can be retrieved from our measurements (Table 2).

Table 2

	$DOX^{®}_{mol}$	$DOX^{®}_{mol\text{-}ex/in^{\chi}}$
DOX_f (%)	**1.37±0. 22**	*Ex:* 0.89±0.16
		In: 0.48±0.10
DOX_b (%)	**0.66±0.08**	*Ex:* 0.25±0.06
		In: 0.41±0.07
DOX_c (%)	**97.98±0.29**	97.98±0.29

Table 2*. In the Column "DOX®mol" are reported the molecular fraction of the three pure species (respectively from the top to the bottom DOX_f, DOX_b and DOX_c). In the second column are reported the final molar fraction of the three pure species divided in the fraction of the drug inside and outside the lisposome.*

4.2 On the uncertainty propagation in the conversion of fractional intensities to molar fractions.

The uncertainty on the QY (QY_i) was calculated considering it to be the standard error on n_i independent measurements (n_f =3, n_c =6). Instead, the uncertainty of QY_b was calculated by standard propagation of independent uncertainties, and it was considered non-correlated with the other uncertainties. The extinction coefficient for DOX_f (ε_f) was obtained from the corresponding fraction of light absorbed by the samples (A_s) by applying the Lambert-Beer relation for an optical path length of 1 cm. The uncertainty is the standard error on n=3 independent experiments. The extinction coefficient for DOX_b (ε_b) was estimated to have value and uncertainty as DOX_f, but the uncertainty was considered uncorrelated. The extinction coefficient for DOX_c (ε_c) was calculated from the corresponding A_s however Confocal and AFM acquisition of the samples showed that the thickness of the layer of the crystal was non-

homogeneous. For this reason, it was applied the Lambert-Beer relation on sample with non-homogeneous path length:

$$T = \frac{\iint_S I_0(x,y)10^{-\varepsilon_c c l(x,y)}dxdy}{\iint_S I_0(x,y)dxdy} = \frac{\iint_S 10^{-\varepsilon_c c l(x,y)}dxdy}{S} \qquad Eq.4.1$$

Where T= 1-A_s is the average transmittance of the area S, c is the concentration of DOX in the crystal, found with a calculation based on the available crystallographic data[99] (c=2.52 M), l(x,y) is the thickness of the crystal layer at point (x,y), $I_0(x,y)$ is the intensity of the incoming light at the point (x,y) within the illuminated area S. For the last equivalence I_0 within S was considered as a constant. Having sampled $l(x,y)$ at different point p using the AFM, the Eq. 4.1 becomes:

$$T = \frac{\sum_p 10^{-\varepsilon_c c l_p}}{n_p} \qquad Eq.4.2$$

Where l_p is the height of the crystal at the pixel p and n_p is the total number of pixels taken in consideration. The sample used for the AFM measurement was the same used for the integrating sphere. We measured the transmittance T in $n_T = 3$ independent measurement on the same samples, as described above. We used the Symbolic Math Toolbox in MatLab (Math-Works® to solve the Eq. 4.4 for ε_c for the three obtained value of T for the three AFM images; then we have been able to calculate the average ε_c^T and standard errors $\sigma_{\bar{\varepsilon},T}$ on the three AFM measures for the three T measures, and a weighted average of the three results has been made:

$$\varepsilon_c = \left. \sum_T \frac{\varepsilon_c^T}{\sigma_{\bar{\varepsilon},T}^2} \middle/ \sum_T \frac{1}{\sigma_{\bar{\varepsilon},T}^2} \right. \qquad Eq.4.3$$

With the final uncertainty value given by the square root of:

$$\sigma_{\bar{\varepsilon}_c}^2 = \frac{1}{\sum_T \frac{1}{\sigma_{\bar{\varepsilon},T}^2}} + \frac{\sum_T (\varepsilon_c^T - \varepsilon_c)^2}{(n_T - 1)n_T} \qquad Eq.4.4$$

To have an additional proof, the order of the operation has been inverted and the results for average ε_c and $\sigma_{\bar{\varepsilon}_c}$ where almost the same (7510±490 $M^{-1}cm^{-1}$ by averaging first on AFM acquisitions and then on the T values and 7500±480 $M^{-1}cm^{-1}$ by carrying out the operation in the opposite order). Then were calculate the three values of brightness $\alpha_i = \mathrm{QY}_i * \varepsilon_i$, and the uncertainties $\sigma_{\bar{\alpha}_i}$ were obtained by standard propagation of independent uncertainties. The fractional-intensity contribution $F_{i,f}$ for the three subpopulations of DOX have been measured in $n_f = 24$ independent experiment. F_i in the average over f of the $F_{i,f}$, and the covariance matrix between these values has been obtained as follows:

$$\sigma_{F_i F_j} = \frac{\sum_f (F_{i,f} - F_i)(F_{j,f} - F_j)}{n_f - 1} \qquad Eq.4.5$$

The molar fractions can be calculated as:

$$F_i^{corr} = \frac{F_i}{\alpha_i} \Big/ \sum_j \frac{F_j}{\alpha_j} \qquad Eq.4.6$$

And the uncertainties:

$$\sigma_{F_i^{corr}}^2 = \sum_{\gamma,\delta} \frac{\partial F_i^{corr}}{\partial \gamma} \frac{\partial F_j^{corr}}{\partial \delta} \sigma_{\gamma\delta}$$

$$= \sum_i \left(\left| \frac{\partial F_i^{corr}}{\partial \alpha_i} \right|^2 \sigma_{\bar{\alpha}_i}^2 + \left| \frac{\partial F_i^{corr}}{\partial F_i} \right|^2 \sigma_{F_i}^2 \right) + \sum_{i>j} 2 \frac{\partial F_i^{corr}}{\partial F_i} \frac{\partial F_j^{corr}}{\partial F_i} \sigma_{F_i F_j} \qquad Eq.4.7$$

with γ, δ in $(\{\alpha_i\}, \{F_i\})$ and, in general, $\sigma_\gamma^2 = \sigma_{\gamma\gamma}$ and $\sigma_{\gamma\delta} = 0$ for uncorrelated entities. Interestingly, if we take in consideration only two species, the sum of the two fractions must be 1, this means that the two fraction are anti-correlated (the two variances are the same, and the covariance is the opposite of the variance); so, it is possible to use the following equation:

$$F_i^{corr} = \frac{F_i}{\alpha_i} \Big/ \left(\frac{F_i}{\alpha_i} + \frac{1 - F_i}{\alpha_j} \right) = \left[1 + \frac{\alpha_i}{\alpha_j} \left(\frac{1}{F_i} - 1 \right) \right]^{-1} \quad (i \neq j) \qquad Eq. 4.8$$

And the Eq. 4.7 with the three uncorrelated variables F_i, α_i, α_j. In all cases, we calculated the uncertainties on the final quantities as expected from single measurements, equivalents to the standard deviation for a population. Consequently, for the F_i it was used the standard deviation, but we use the statistical uncertainty on the true value of the α_i parameters (corresponding to the standard error). Wort of note is that in our experiments the presented uncertainties reflect only the statistical one. The approximations used could give rise to systematic errors. For examples we considered the interaction of light with DOX_b and DOX_f to be the same, taking into account only a weaker non-radiative decay for the membrane-bound form. Furthermore, we were not able to check if crystal deposited on the gals and organized in a web of nano-strips has the same density of the bulk crystal or if this nano-structure have a different and maybe more complicated effect on the light wave (due to diffraction and refraction) than the one expected from a typical application of the Lambert-Beer law. The QY of a mixture of different species (QY_{mix}) can be calculated as

$$QY_{mix} = \frac{\sum_i \varepsilon_c F_i^{corr} QY_i}{\sum_i \varepsilon_c F_i^{corr}} = \frac{\sum_i F_i}{\sum_i F_i / QY_i} = \left(\sum_i \frac{F_i}{QY_i} \right)^{-1} \qquad Eq. 4.9$$

And its uncertainty can be obtained an equation similar to Eq. 4.7. A final round of data analysis was carried out on the independent experiment performed using

KI as a quencher of DOX, with the goal of identifying the fractions of DOX_f and DOX_c exposed to the external solution (assuming that the KI cannot affect DOX_c or the fraction of DOX_f and DOX_c buried within the lipidic membrane of the nanoparticles). Thus, the measured fractions of either DOX_f or DOX_b in presence of KI ($F_i^{post\ KI}$) were corrected considering the apparent slight variation detected in the fractional-intensity contribution of DOX_c according to:

$$F_i^{post\ KI-corr} = F_i^{post\ KI} * \frac{F_c^{pre\ KI}}{F_c^{post\ KI}} \qquad Eq.\ 4.10$$

The percentage of both DOX_f or DOX_b exposed to inner side of the nanoparticle membrane are easily derived, according to:

$$\%F_i^{int} = \frac{F_i^{post\ KI-corr}}{F_i^{pre\ KI}} \times 100 \qquad Eq.\ 4.11$$

From the experiments with KI used as a quencher: after addition of KI, 65.1 ± 4.3% of the free form is switched off; 37.9 ± 6.9% of the membrane-bound form is switched off.

4.3 Concluding remarks on Doxil® synthetic identity

We were able to develop a new analytical tool that allows, with a nano-scale precision, to identify and quantitatively determine the sub-molecular organization of the DOX (or any kind of drugs having an intrinsic fluorescence signal) within the liposomes (schematic in Fig. 4.8). As discussed in Chapter 1 and citing verbatim Y. Barenholz "in Doxil® each component matters and contributes to optimized performance". Based on the results showed in this research we argue that quantifying the different fraction is an important step

towards the understanding of the performance and the monitoring of encapsulated DOX both *in vivo* and *in vitro*.

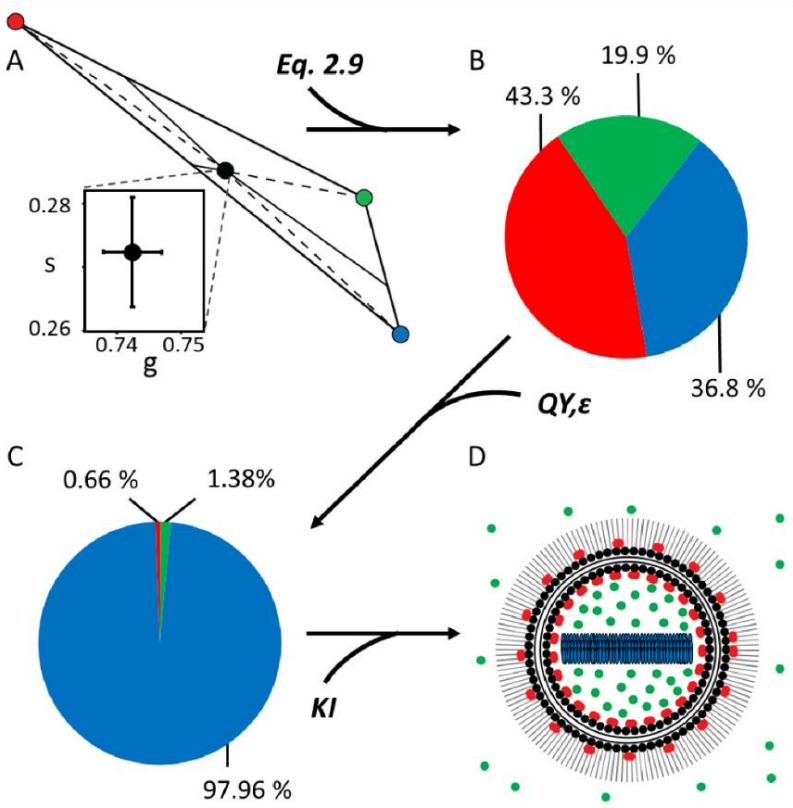

Fig. 4.8 ***Quantification of the molar fractions of the three DOX species within DOX®:*** *Schematic summary of our approach: from the lifetime data to the complete model of DOX®. A) a schematic phasor representation of our FLIM data and the rules to find the fractional-intensity contributions of the three DOX species within DOX®. B) The corresponding pie-chart. C) Pie-chart representing the molar fractions of the different species after correction by QY and ε. (D) Schematic model of DOX® based on phasor-FLIM results, including KI-based ones: green dots are DOX_f both as non-encapsulated and encapsulated; red dots are DOX_b, associated to both membrane layer; in blue is represented the DOX_c, buried in the liposome core.*

We strongly believe that this approach can be easily applied to the study of the super-molecular organization of a wide range of nano-drugs, with different advantages with respect to standard methodologies: (i) it is a label free procedure, there is no necessity of modifying chemically the sample under investigation but it is exploited its intrinsic signal; (ii) it uses a fast, fit-free data analysis procedure; (iii) it has a high sensitivity at the nanoscale in standard optical setup. Related to this latter point: the use of visible light makes the proposed platform particularly promising for investigating how a drug 'synthetic identity' may change upon interaction with living matter, at any level, from bodily fluids (e.g. by the adsorption of proteins from the blood serum) to the intracellular environment. Finally, we envision similar applications in adjacent fields to provide fast readouts in quality tests along the production line of substances such as agrochemicals (e.g. controlled-release pesticides), industrial chemicals (e.g. paints, adhesives, inks, anti-counterfeiting inks, cosmetics), textiles, nutraceutical/dietary supplements.

5

Future perspectives: from synthetic identity to biological function of encapsulated DOX

5.1 From synthetic to biological identity

The use of nanocarriers, such as liposomes, as drug delivery vectors for therapeutic agents and in particular for chemotherapeutic drugs offers a means for increase drug efficacy and reduce cytotoxicity by modulating the drug distribution. A precise understanding and the quantification of the drug nanoscale structure, organization and phase within the nanoparticle is one of the major obstacles to overcome and would facilitate the development and the approval of new drug formulations. The proposed approach can be used for the investigation of several molecules as far as they have a fluorescence signal (even a weak one). It is known that when liposomal drugs enter a physiological environment, their surface gets coated by a dynamic biomolecular corona (BC)[100–105] that covers nanocarriers *in vivo*, changes their synthetic identity, changes in time[106] and has a deep impact on the particle fate[107–109]. In liposome research the impact of BC has been long underestimated[110] because grafting PEG to liposome surface was generally assumed to inhibit protein adsorption, and consequently keep liposome functionality intact. Recently, it was clarified that PEGylation mitigates protein binding, but does not avoid BC formation[111,112]. One of the most important implications is that clinically approved liposomal formulations could not be stealth *in vivo*. Since protein adsorption is not preventable on PEGylated liposomes, what the patient's cells actually "see", when coming in touch with liposome, is liposome's BC and not the pristine vesicle[113,114]. The recognition of specific epitopes could have a deep impact on several biological processes, such as association with cell receptors, liposome accumulation at the target site, cell internalization, drug release and intracellular trafficking. Kostarelos et al. were the first to confirm that after administration to mice Doxil® is covered by a BC[115]. However, following exposure of liposomes to mouse (MP) and human plasma (HP), resulting coronas were found to differ both in number and abundance of

identified proteins[116] . This result indicated that physiological outcome of liposomes in animal models such as pharmacokinetic (PK) and body distribution (BD) could be largely different from those in humans. To date, this gap makes it difficult to translate results obtained on animals into the clinic[117]. Accurate understanding of the human liposome-BC could contribute to explain the limited clinical success of liposomal DOX[118]

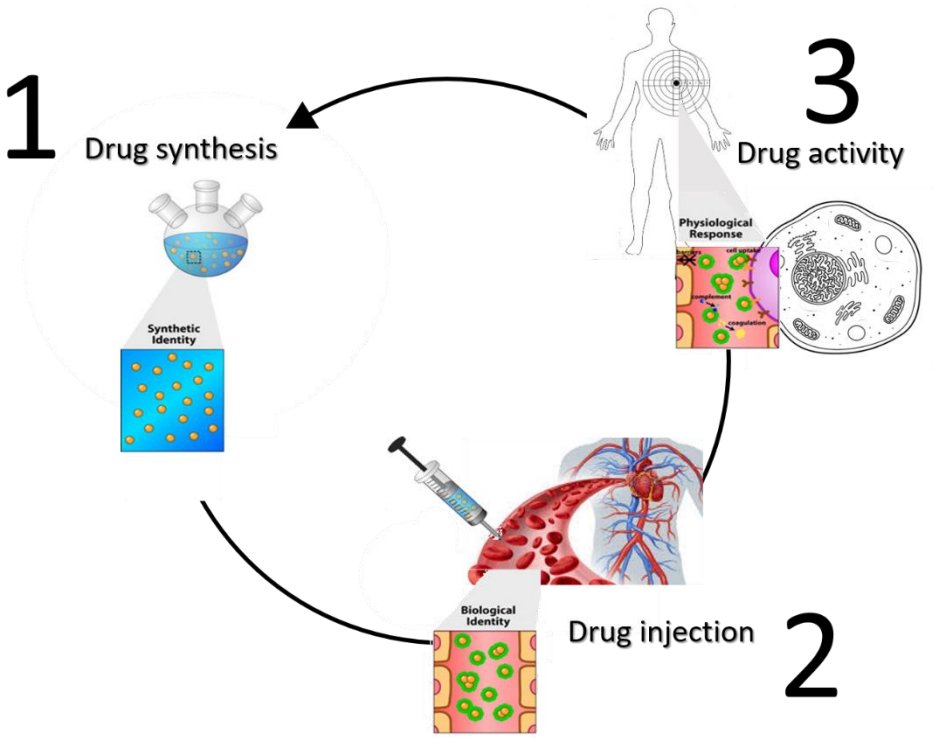

Fig 5.1 ***Schematic representation of the fate of nanoparticles once administrated intravenously****: 1) the Synthetic Identity of the nanoparticles when they are Synthetized. 2) during intravenous administration the interaction with the hemato-protein (i.e. BC formation) change the Synthetic Identity of the nanoparticles to the so called "Biological Identity". 3) The activity of the drug it is now strictly related to its new Biological Identity.*

To test this hypothesis, in collaboration with the group of Prof. Giulio Caracciolo at the University of Rome "La Sapienza", a comprehensive investigation of the synthetic identity, biological identity and cellular response to liposomal DOX was performed[118].

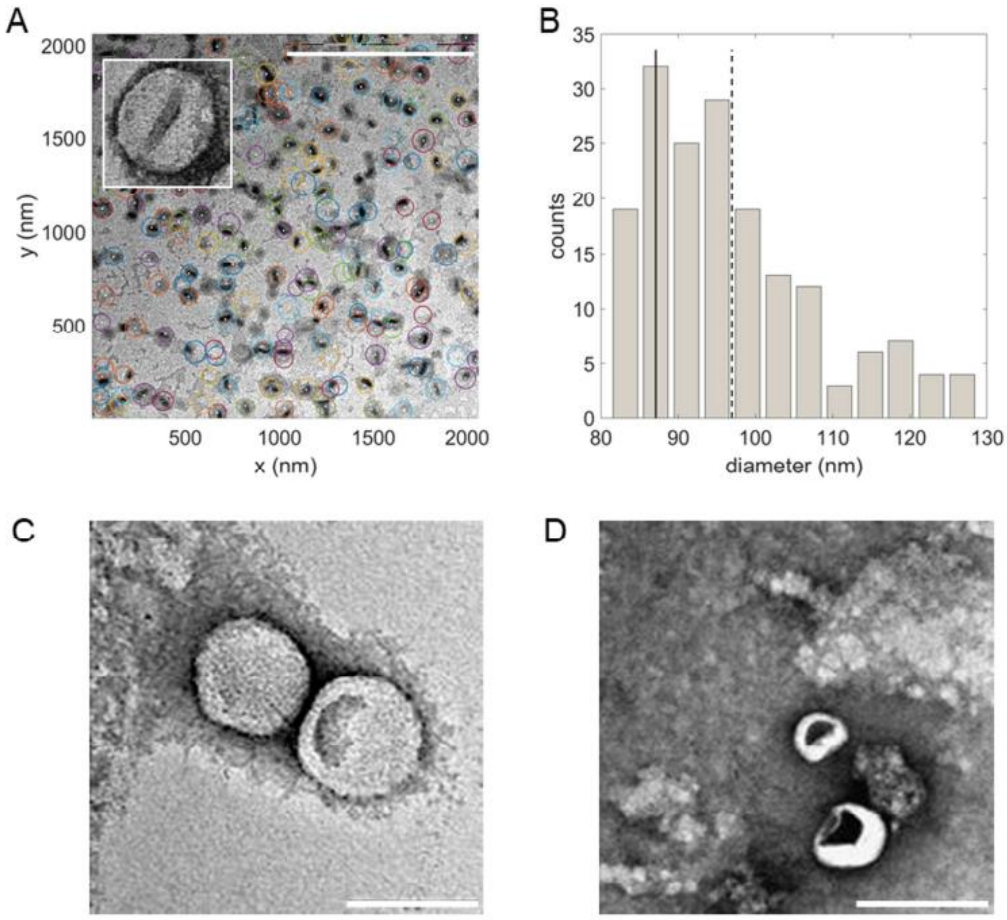

Fig 5.2 ***Transmission electron microscopy (TEM) image of DOX®;*** *A)Scale bar: 1 micrometer. long and fiber-like crystals of DOX are clearly shown in the inset. B) Size distribution of Doxoves®. Solid and dashed lines indicate median and average of size distribution respectively C) Representative TEM images of DOX®-HP complexes (HP=50%). Scale bar: 100 nm D) TEM images of broken DOX®. Scale bar: 200 nm.*

Bilayer structure of DOX® was investigated by synchrotron SAXS that is the method of choice for the structural characterization of materials at the nanoscale, and it is commonly used for the study of liposomes[119]. Synchrotron SAXS scans of DOX®-HP complexes showed diffuse scattering that is characteristic of positionally not correlated bilayers[119], while diffraction Bragg peaks were not detected. This means that protein binding does not promote formation of multilamellar structure as those found in cationic liposome-HP complexes [120]. TEM images (Fig. 5.2, panel A) show that DOX® liposomes are pretty homogeneous in size. As TEM images clearly show, DOX is aggregated in the form of one-dimensional (1D) rod-like crystals. According to literature[45], DOX rods can touch the lipid bilayer, inducing formation of non-spherical vesicles. TEM images for DOX® after incubation in HP are reported in Fig. 5.2, panel C. First, no trace of multilamellar aggregates was found. This finding was consistent with synchrotron SAXS results. On the other side, TEM images showed the presence of several ruptured vesicles (Fig. 5.2, panel D). This would suggest that, following exposure to HP, DOX® could not be robust enough to keep the liposome integrity. Although the exact molecular mechanisms have not been clarified so far, previous studies showed that DOX crystals touch the vesicle membrane, producing a pressure gradient between the outside and the inside of the particle (reviewed in reference [121]). Such a pressure gradient is likely to break lipid vesicles leading to drug release[122]. A Mass Spectrometer was used for a deeper characterization of the BC adsorbed on DOX®. 239 proteins were identified in the BCs of DOX® by nanoLC-MS/MS at low (HP=5%), medium (HP=20%) and high (HP=50%) plasma concentration. This finding supports the current assumption that the liposome-BC consist of a few hundred proteins[123]. Fig. 5.3 shows the Venn diagrams. A big fraction of proteins, precisely 221, were common to the three BCs; 8 proteins were “unique”, i.e. they were found only in one BC; 6 proteins were in common between two BCs.

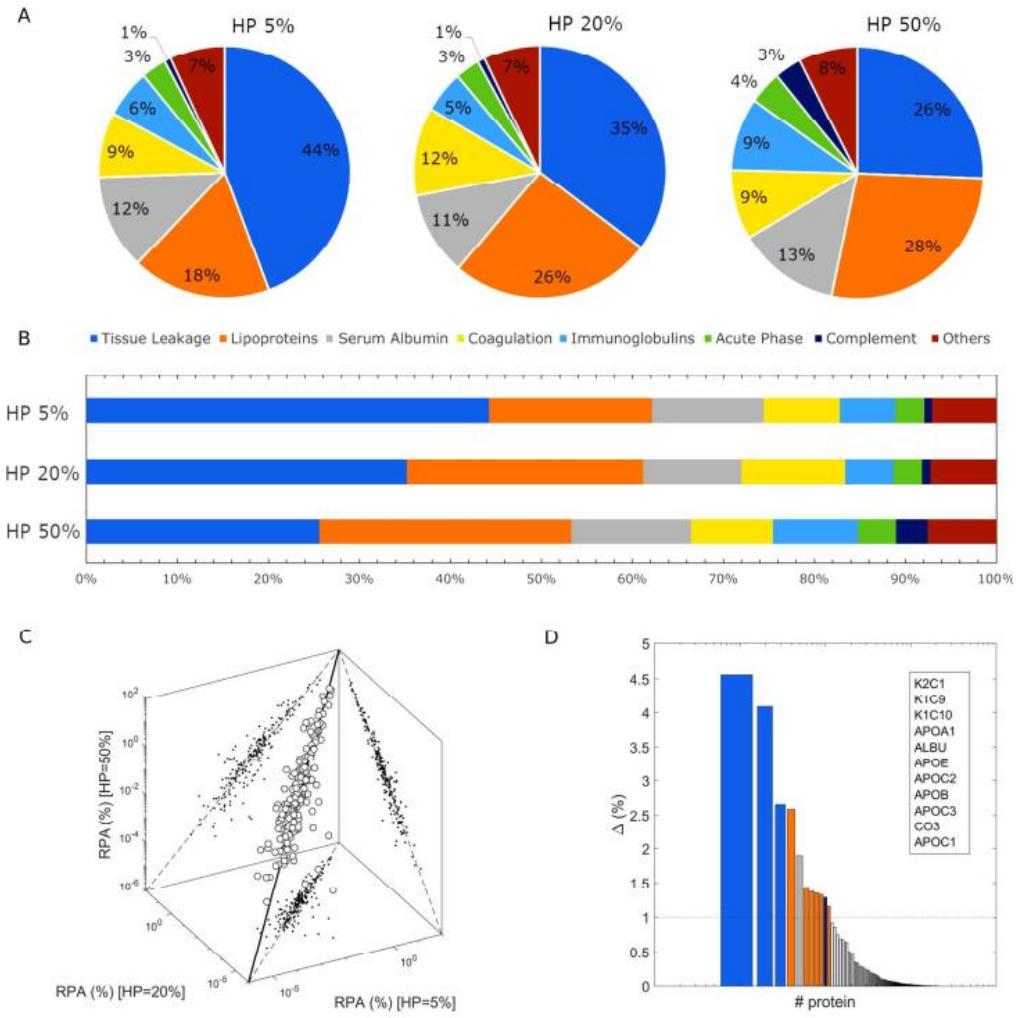

Fig. 5.3 ***Bioinformatic classification of corona proteins found in the biomolecular corona of DOX® after 1 h incubation with human plasma (HP) at 37°C as determined by nanoLC/MS-MS***:. *Proteins were grouped according to their physiological functions at different HP concentration: A) pie charts, B) histograms. C) Scatter plot depicting the measured relative protein abundances under different conditions of plasma concentrations (HP=5%, HP=20%, HP=50%). The diagonal represents an ideal reference distribution of data points with equal protein abundances under the investigated conditions. D) Distance\Delta between each of the experimental data points and the reference diagonal. Results are sorted in descending order to rank the identified corona proteins according to their sensitivity to the plasma concentration*.

Plasma proteins were grouped according to their physiological functions (Fig. 5.3). Of note, typical "opsonins" such as immunoglobulins (RPA < 10 %) and complement proteins (RPA < 5 %) were poorly abundant in the corona of DOX®–HP complexes. On the other side, DOX® avidly bind serum clotting factors (e.g. Fibrinogen) and Apolipoproteins (15% < RPA < 30%). Comparing "coronome" of DOX® (Fig. 5.3) with that of empty liposomes, systematic differences were found. Thanks to our FLIM approach now we can confirm that a fraction of DOX is located at the vesicle surface, so this discrepancy in corona composition is probably due to the presence of the drug that is competing with lipids for protein binding.

5.2 From biological identity to functional identity: preliminary tests on cultured cells

Once the synthetic identity of DOX® was defined, we decided to use the phasor-FLIM approach to observe the drug upon interaction with living matter, in a simplified *in vitro* experiment. Our first experiment was a classic confocal imaging on live cells *in vitro*, conducted in a way to confront the free drugs and the liposomal formulation DOX®. To evaluate the delivery of the drugs we chose to conduct the experiment in an ideal environment, so the incubation with drug, both in the free and liposomal form, was done in a medium without plasma, to avoid the problem of the protein corona. The behavior of the liposomal-DOX is completely different from the free form of the drugs (to see in Fig. 5.4) even if the experiments were conducted in the ideal condition; there is a higher accumulation in the cytoplasm and a lower one in the nucleus. To try to get more information about this behavior we decided to replicate the experiment *in vitro* by using the phasor-FLIM approach. FLIM acquisition were made at different

time points and with different typologies of administration (leaving the drugs in the media or washing it after 2h of incubation).

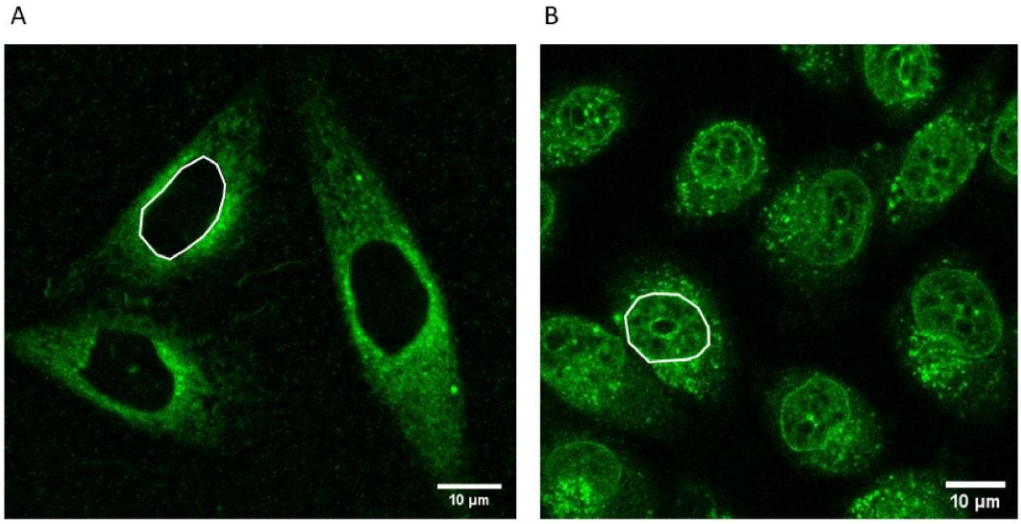

Fig. 5.4 ***DOX vs DOX®:*** *CHO-K1 cells after 20 minutes of incubation with Doxoves® (A) and free DOX (b). The final concentration of DOX was 12 µg/mL in both experiments.*

The data from these experiments are not yet conclusive, but an example is showed in Fig. 5.5. In conclusion, fluorescence lifetime proved to be a powerful tool to characterize pharmaceutical nano vectors. Indeed, the fluorescence proprieties of a molecule can be affected by the surrounding environment. Therefore, with the proposed Phasor FLIM approach it would be possible unveil information on different aspects of the nano-formulations, from the synthetic identity to the releasing mechanism of drugs. Furthermore, similar applications can be exploited to overcome the quality criteria imposed by the Competent Authorities to make the formulations suitable for market authorization. Indeed, it can be a fast and robust method to perform quality tests along the production chain as well as the storage of different molecules, thus making the FLIM approach appealing for

applications in pharmaceutical, agrochemical, industrial chemical, nutritional/dietary supplement and textile fields.

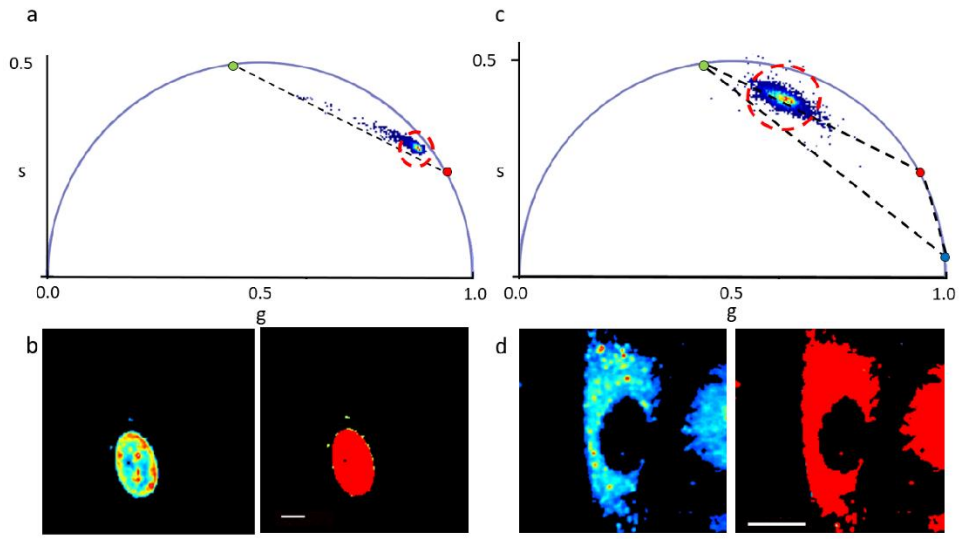

Fig. 5.5 ***Lifetime fingerprint of DOX vs DOX®:*** *a) Phasor plot of CHO-K1 cells incubated with DOX for 4h and washed with PBS. The red dot represents the lifetime value of 1 (i.e. DOX_f); the green dot represents the lifetime value of DOXc (i.e DOX_f interacting with the cellular membranes). As it is possible to see the phasors of nucleus (highlighted by the dashed red circle) are above the conjunction line for the two species, this shift it is probably due to the intercalation of the drugs with the DNA. b) and Life-Time imaging of the cell (scale bar 10 µm). c) Phasor plot of CHO cell incubated with Doxil® for 4h and washed with PBS. The higher concentration of phasors lies closest to the green dot (i.e. DOXc) suggesting that the drugs in this phase is interacting with the cellular membrane. c) and Life-Time imaging of the cell (scale bar 10 µm)*

5.3 DOX absorbed on Graphene Oxide

We tested out the phasor-FLIM approach with other nano-delivery tools. The first, produced in laboratory of Prof. Giulio Caracciolo at the University Sapienza of Rome, is the so-called GO-DOX (Graphene Oxide DOX) [124]. Indeed, their aim was to overcome the limitation of Liposomal-DOX formulation by developing a novel nano-carrier for the drugs. The Graphene Oxide (GO) is indeed considered

a promising carrier due to its peculiar physical–chemical properties such as high surface area, high water dispersibility and good biocompatibility [125]. Compared to other nanocarriers, GO exhibits favorable drug loading capacity due to the two-dimensional planar arrangement of carbon atoms that allows a total exposure of functional groups to the chemical surrounding[126]. Moreover, epoxydic and carboxylic groups on the GO surface can be used to selectively bind drug molecules, thus enhancing drug solubility in aqueous media [127–129]. On the other side, lateral dimensions of GO nanosheets have limitations regarding blood–brain transport, renal clearance, biodegradation and toxicity that have substantially impaired its clinical application so far[130,131]. Our contribution was to investigate by standard confocal imaging, and exploiting DOX intrinsic fluorescence, how the GO promotes intracellular delivery and subsequent nuclear accumulation of DOX molecules and that such an outcome is followed by high anticancer activity. By phasor-FLIM analysis, we were able to characterize both the "synthetic identity" of GO-DOX nanosheets (Fig. 5.6 A-B) and their behavior in a cellular environment *in vitro*. We performed phasor-FLIM analysis on cells treated with GO-DOX and with free DOX as control (Fig. 5.6 D-F). As somewhat expected, the characteristic lifetime signature of free DOX transforms into a broad distribution of multi-component lifetimes upon interaction (and mixing) with the complex ensemble of extracellular and intracellular auto-fluorescent species, which are multi-exponential in nature[132]. In particular, two sub-clusters are easily recognizable in the phasor plot, one corresponding to DOX molecules localized in the nucleus (red circle in Fig. 5.6 C, red pixels in Fig. 5.6 D), another corresponding to DOX molecules localized in the cytoplasm (green circle in Fig. 5.6 C, green pixels in Fig. 5.6 D). Please note, also, that the lifetime of DOX in the nucleus is close to that of free DOX in water (indicated by the red point in Fig. 5.6 C, E) while, by contrast, DOX lifetime in the cytoplasm shows a sensibly different distribution pattern that can be reasonably ascribed to interaction of

DOX with biological membranes (DOX associated to surfaces, in fact, is known to have a lifetime similar to that extrapolated here from data and located at approximately 4 ns [133], green point in the phasor plot in Fig. 5.6 C).

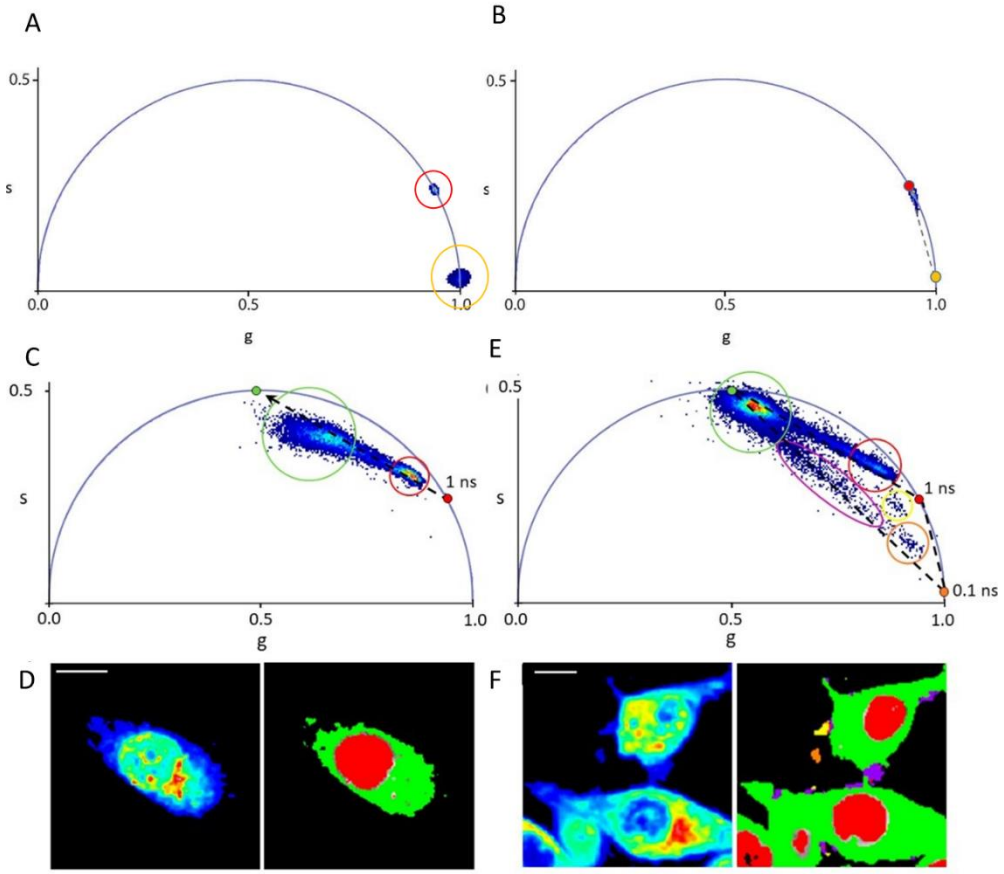

Fig. 5.6 ***Phasor FLIM analysis of MDA-MB 231 cell exposed to DOX and GO-DOX****:*
A) The red circle highlights the experimental lifetime of DOX in aqueous solution (1 ns). The yellow circle highlights the experimental lifetime of pristine graphene-oxide (GO) in aqueous solution. B) The experimental cluster of GO-DOX is a linear combination of the two components, GO and DOX (represented by the red and yellow dots). C) Phasor representation of lifetimes measured in cells exposed to DOX. The phasor plot contains clouds of points that correspond to pixels with similar lifetime spectra. These clouds can be selected by specific regions of interest (ROIs). The green ROI, for instance, highlights the portion of pixels corresponding to DOX in the cytoplasm (see right panel in 'D', the cytoplasm is colored in green); the red ROI clearly identifies pixels corresponding to DOX in the nucleus (see right panel in 'D', the nucleus is colored in red); a dashed line is drawn across the phasor distribution and used to extrapolate the

hypothetical position of a pure species on the universal circle (green point located at 4 ns) presumably corresponding to DOX associated to membranes. D) Intensity (left) and lifetime (right) images of a MDA-MB 231 cell exposed to DOX (the same analyzed in (C)). The lifetime image is colored according to the ROIs in (C). E,F) Same as before but for MDA-MB 2311 cells exposed to GO-DOX. Please note that the phasor-FLIM signature of cytoplasmic (green cursor in 'E', green pixels in 'F') and nuclear DOX signals (red cursor in 'E', red pixels in 'F') show clear similarity to that obtained for free DOX. By contrast, as expected, additional signals are present here, which are absent in cells treated with free DOX. In particular, as highlighted by the violet, orange and yellow cursors in 'E' (and pixels of the same color in 'F') there are micrometric patches, mostly associated with cell membranes, with variable amounts of the nude carrier (GO) and the released drug (both free or associated to cellular membranes). Scale bars: 10 μm.

What is important for the purpose of this work, however, is that GO-DOX shows some relevant similarities with free DOX in terms of phasor-FLIM signatures within the cell. In particular, the same phasor-plot features described for free DOX are found in cells treated with GO-DOX: an elongated overall distribution with one subcluster corresponding to nuclear DOX (closer to DOX in water, highlighted in red) and another corresponding to cytoplasmic DOX (closer to DOX adsorbed to surfaces/membranes, highlighted in green; Fig. 5.6 E).

Of note, the lifetime analysis unveils sites of putative GO-DOX attachment to the cell surface (and subsequent drug release), which are not visible in the intensity image (reported in Fig. 5.6 F, left panel). As highlighted in Fig. 5.6 E, the most important difference in the lifetime data from cells treated with GO-DOX is the presence of pixels with sensibly shorter lifetimes, in particular pointing towards the lifetime of nude GO (i.e., 0.1 ns, orange point). The triangle with vertices the lifetime of the three "pure" species (free DOX, DOX associated to membranes and nude GO) can represent a framework guiding data interpretation. As mentioned above, the phasor data lying along the line between free DOX and membrane-associated DOX recapitulates the main features observed treating cells with free DOX and can be interpreted as an indication that the drug is effectively released at the intracellular level. By contrast, data along the lines

connecting nude GO with the other two species unveil the presence of pixels in the image where a variable amount of the carrier (GO) and the released drug (both free or associated to cellular membranes) is detected. We separated this population of pixels into subpopulations of a different color (see violet, orange and yellow cursors in Fig. 5.6 E). Of note, however, they all concur to highlight selected micrometric patches on the cell border (Fig. 5.6 F). We are prompted to ascribe these patches to sites of GO-DOX cell attachment and subsequent drug release (Fig.5.6). This observation is in agreement with recent findings obtained using graphene decorated with cyclodextrins and loaded with DOX[134]. The authors, in fact, also due to lifetime analysis, evidenced the efficient cellular uptake of the whole adduct and the presence of DOX in the nucleus without the graphene carrier. From a methodological point of view, our results corroborate the idea that FLIM can represent a quantitative platform to analyze DOX cellular uptake and release from nanocarriers, in line with a growing body of evidences from the literature [133,135,136].

5.4 DOX chemically linked to *Listeria monocytogenes*

The same approach was used also with other example of vector, this time thanks to the collaboration with the laboratory of Dr. Laura Poliseno at CNR-IFC, Pisa. They optimized a strain of attenuated *Listeria monocytogenes* (Lm^{at}) capable of delivering DOX in tumoral cells. Indeed, it is demonstrated that Lm^{at} can be a valuable tool to create an anticancer vaccine, thanks to its intrinsic properties capable of triggering the immune response against tumoral cells [137]. Furthermore, Lm^{at} presents different advantages: they are able to accumulate in a selective way inside cancer tissue and it can reach also the deeper region of the tumor by spreading cell to cell. Since it is easily manipulable genetically, it has been widely exploited as a carrier for different biomolecules such as therapeutic enzymes[138],

nucleic acids [139] and peptides[140]. The aim of this work was to engineering Lm^{at} strains as a carrier for molecules non-encoded in the genetic materials such as DOX to enhances the anti-tumoral activity. In this work for the labelling of Lm^{at} was used an approach consisting in two steps: the first one is the integration of alkyne-bearing D-alanine in peptidoglycan peptide, the second one was the attachment, via covalent bound, of azide-bearing DOX by Copper-catalyzed Azide-Alkyne Cycloaddition (or CuAAC). This approach was already optimized in other works [141–143] and it was demonstrated to be biocompatible, key characteristics since Lm^{at} can have an anti-tumoral effect only if it is alive. In this work it was tested the introduction of both alkine-modified D-alanine and alkyne-D-alanine-D-alanine probe for the labelling, respectively, the fifth and the fourth D-alanine of the peptidoglycan (Fig. 5.7).

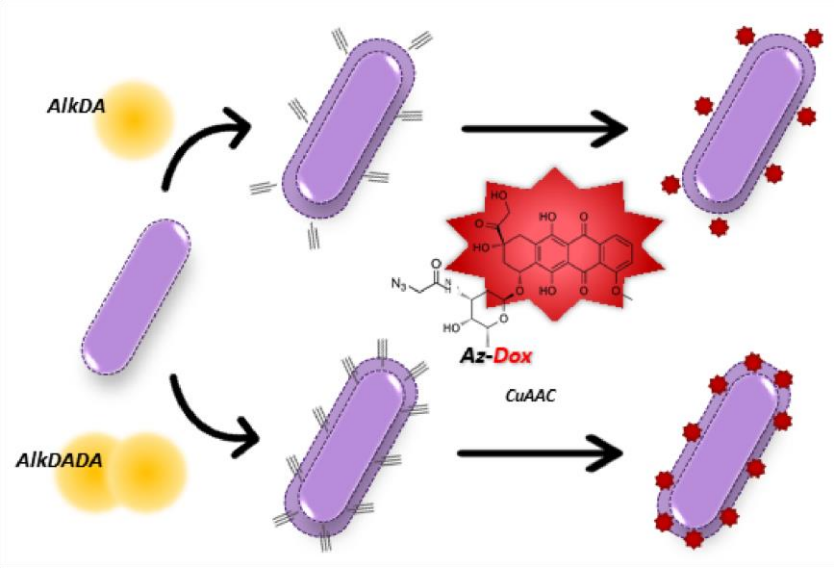

Fig. 5.7 ***Schematic representation of the approach the functionalization of Lm^{at} with DOX:*** *Lm^{at} is pre-incubated with AlkDA (top left) or AlkDADA (bottom left) probes to generate Alk-Lm^{at}. After the CuAAC reaction with the Azide-bearing DOX on the fifth (top right) or fourth (bottom right) position of the peptidoglycan a Dox-Lm^{at} it is generated.*

The structure of Dox was modified in the primary amine on the aminoglycoside portion by functionalization with an azidoacetic group producing azido-DOX, suitable for the CuAAC reaction. Our contribution to the work was to use the phasor-FLIM approach to characterize the success of the attachment of DOX on the surface of the Lm^{at} and to demonstrate that the labeling of the bacteria was essential to the functionalization of Lm^{at} with DOX. As it is possible to see in Fig.5.8, we performed FLIM on different samples: first of all, we run experiment on the Azide-DOX (red circles) and Lm^{at} (light blue circle), obtaining the respective phasors. Then we acquired the lifetime of two different samples undergoing to the CuAAC reaction: the first one was Lm^{at} non treated with the probe (orange circle) and a second one with the probe (yellow circle). The experiments were conducted with both AlkDA-Lm^{at} (Fig. 5.8 A) and AlkDADA-Lm^{at} (Fig. 5.8 B), and the results are similar: the phasors of the sample with the Lm^{at} treated with the probes and then conjugated with azide-DOX are along the conjunction line of the cluster of az-DOX and the autofluorescence signal of the nude Lm^{at}, demonstrating the functionalization of the bacteria.

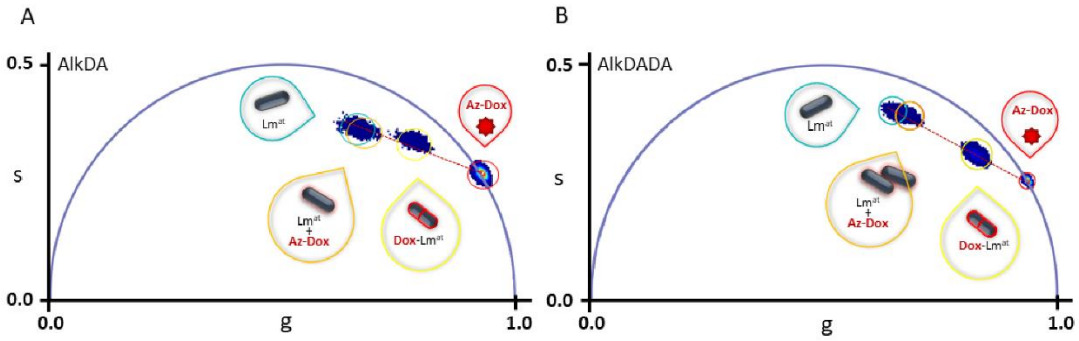

Fig. 5.8 ***Phasors plots related to Lm^{at} labelled by using AlkDA A) or AlkDADA B) as probe:*** *We can find from left to right: Lm^{at} nude bacteria (light blue circle), Lm^{at} not without the probe but incubated with DOX and underwent CuAAC reaction (orange circle), Lm^{at} treated with the probes and incubated with DOX and underwent CuAAC reaction (yellow circle), Azide-DOX (red circle).*

The phasors of the sample in which the Lm^{at} was not treated with the probes are almost superimposable with the phasors of the nude bacteria, meaning that the conjugation didn't happen. The difference between the phasors of AlkDA-Lm^{at} and AlkDADA-Lm^{at} lies on the distance from the phasors cluster of the two "pure species" (i.e. Lm^{at} and az_DOX): in the AlkDADA-Lm^{at} case the cluster is nearer to the az-cluster, indication an higher functionalization, data that was supported by other experiment in the work.As is possible to see from these examples, this approach can give fast and qualitative characterization of different kind of vectors, the only requirement is that they must have a fluorescence signal, even if it is really weak (for example the cellular autofluorescence).

References

1. BLUM RH. Adriamycin. A new anticancer drug with significant clin-ical activity. *Ann Intern Med*. 1974;80(2):249. doi:10.7326/0003-4819-80-2-249

2. Mckelvey EM, Cottljeb JA, Wilson HE, et al. *HYDROXYLDAUNOMYCIN (ADRIAMYCIN) COMBINATION CHEMOTHERAPY IN MALIGNANT LYMPHOMA*. Vol 38.; 1976.

3. Gundersen S, Kvinsslasd S, Klepp T 0, Zl@y SK, H@st H. *Weekly Adriamycin Versus VAC in Advanced Breast Cancer. A Randomized Trial*.

4. Arcamone F, Cassinelli G, Fantini G, et al. Adriamycin, 14-hydroxydaimomycin, a new antitumor antibiotic fromS. Peucetius var.caesius. *Biotechnol Bioeng*. 1969;11(6):1101-1110. doi:10.1002/bit.260110607

5. Sun J, Wei Q, Zhou Y, Wang J, Liu Q, Xu H. A systematic analysis of FDA-approved anticancer drugs. *BMC Syst Biol*. 2017;11(S5):87. doi:10.1186/s12918-017-0464-7

6. Sritharan S, Sivalingam N. A comprehensive review on time-tested anticancer drug doxorubicin. *Life Sci*. 2021;278:119527. doi:10.1016/j.lfs.2021.119527

7. Hahn GM, Braun J, Har-Kedar I. Thermochemotherapy: synergism between hyperthermia (42-43 degrees) and adriamycin (of bleomycin) in mammalian cell inactivation. *Proceedings of the National Academy of Sciences*. 1975;72(3):937-940. doi:10.1073/pnas.72.3.937

8. Speth PaulAJ, Linssen PeterCM, Boezeman JanBM, Wessels HansMC, Haanen C. Cellular and plasma adriamycin concentrations in long-term

infusion therapy of leukemia patients. *Cancer Chemother Pharmacol*. 1987;20(4). doi:10.1007/BF00262581

9. Yang F, Teves SS, Kemp CJ, Henikoff S. Doxorubicin, DNA torsion, and chromatin dynamics. *Biochimica et Biophysica Acta (BBA) - Reviews on Cancer*. 2014;1845(1):84-89. doi:10.1016/j.bbcan.2013.12.002

10. Rahman A, Kessler A, More N, et al. *Liposomal Protection of Adriamycin-Induced Cardiotoxicity in Mice1*. http://aacrjournals.org/cancerres/article-pdf/40/5/1532/2407527/cr0400051532.pdf

11. Schein P. *Pharmacological, Toxicological, and Therapeutic Evaluation in Mice of Doxorubicin Entrapped in Cardiolipin Liposomes*.; 1985. https://www.researchgate.net/publication/19195189

12. Rahman A, Fumagalli A, Barbierp B, Schein PS, Casazza AM. *Ancer Hemotherapy and Harmacology Antitumor and Toxicity Evaluation of Free Doxorubicin and Doxorubicin Entrapped in Cardiolipin Liposomes**. Vol 16.; 1986.

13. Rahman A, Carmichael D, Harris M, Roh JK. *Comparative Pharmacokinetics of Free Doxorubicin and Doxorubicin Entrapped in Cardiolipin Liposomes1*. Vol 46.; 1986. http://aacrjournals.org/cancerres/article-pdf/46/5/2295/2426222/cr0460052295.pdf

14. Rochette L, Guenancia C, Gudjoncik A, et al. Anthracyclines/trastuzumab: new aspects of cardiotoxicity and molecular mechanisms. *Trends Pharmacol Sci*. 2015;36(6):326-348. doi:10.1016/j.tips.2015.03.005

15. Volkova M, Russell R. Anthracycline Cardiotoxicity: Prevalence, Pathogenesis and Treatment. *Curr Cardiol Rev*. 2012;7(4):214-220. doi:10.2174/157340311799960645

16. Zhang S, Liu X, Bawa-Khalfe T, et al. Identification of the molecular basis of doxorubicin-induced cardiotoxicity. *Nat Med*. 2012;18(11):1639-1642. doi:10.1038/nm.2919

17. Raj S, Franco VI, Lipshultz SE. Anthracycline-Induced Cardiotoxicity: A Review of Pathophysiology, Diagnosis, and Treatment. *Curr Treat Options Cardiovasc Med*. 2014;16(6):315. doi:10.1007/s11936-014-0315-4

18. Singal PK, Iliskovic N. Doxorubicin-Induced Cardiomyopathy. *New England Journal of Medicine*. 1998;339(13):900-905. doi:10.1056/NEJM199809243391307

19. Zagar TM, Cardinale DM, Marks LB. Breast cancer therapy-associated cardiovascular disease. *Nat Rev Clin Oncol*. 2016;13(3):172-184. doi:10.1038/nrclinonc.2015.171

20. Chiong M, Wang Z v, Pedrozo Z, et al. Cardiomyocyte death: mechanisms and translational implications. *Cell Death Dis*. 2011;2(12):e244-e244. doi:10.1038/cddis.2011.130

21. Whelan RS, Kaplinskiy V, Kitsis RN. Cell Death in the Pathogenesis of Heart Disease: Mechanisms and Significance. *Annu Rev Physiol*. 2010;72(1):19-44. doi:10.1146/annurev.physiol.010908.163111

22. Ghigo A, Li M, Hirsch E. New signal transduction paradigms in anthracycline-induced cardiotoxicity. *Biochimica et Biophysica Acta (BBA) - Molecular Cell Research*. 2016;1863(7):1916-1925. doi:10.1016/j.bbamcr.2016.01.021

23. Komdeur R, Meijer C, van Zweeden M, et al. Doxorubicin potentiates TRAIL cytotoxicity and apoptosis and can overcome TRAIL-resistance in rhabdomyosarcoma cells. *Int J Oncol*. Published online September 1, 2004. doi:10.3892/ijo.25.3.677

24. Bouralexis S, Clayer M, Atkins G, et al. Sensitivity of fresh isolates of soft tissue sarcoma, osteosarcoma and giant cell tumour cells to Apo2L/TRAIL and doxorubicin. *Int J Oncol*. Published online May 1, 2004. doi:10.3892/ijo.24.5.1263

25. Kang J, Bu J, Hao Y, Chen F. Subtoxic concentration of doxorubicin enhances TRAIL-induced apoptosis in human prostate cancer cell line LNCaP. *Prostate Cancer Prostatic Dis*. 2005;8(3):274-279. doi:10.1038/sj.pcan.4500798

26. Wu XX, Kakehi Y, Mizutani Y, et al. Enhancement of TRAIL/Apo2L-mediated apoptosis by adriamycin through inducing DR4 and DR5 in renal cell carcinoma cells. *Int J Cancer*. 2003;104(4):409-417. doi:10.1002/ijc.10948

27. Wang S, Ren W, Liu J, et al. TRAIL and Doxorubicin Combination Induces Proapoptotic and Antiangiogenic Effects in Soft Tissue Sarcoma *In vivo*. *Clinical Cancer Research*. 2010;16(9):2591-2604. doi:10.1158/1078-0432.CCR-09-2443

28. Mizutani Y, Okada Y, Yoshida O, Fukumoto M, Bonavida B. Doxorubicin sensitizes human bladder carcinoma cells to Fas-mediated cytotoxicity. *Cancer*. 1997;79(6):1180-1189. doi:10.1002/(SICI)1097-0142(19970315)79:6<1180::AID-CNCR17>3.0.CO;2-W

29. Massart C, Barbet R, Genetet N, Gibassier J. Doxorubicin Induces Fas-Mediated Apoptosis in Human Thyroid Carcinoma Cells. *Thyroid*. 2004;14(4):263-270. doi:10.1089/105072504323030915

30. Perik PJ, de Vries EGE, Gietema JA, et al. The dilemma of the strive for apoptosis in oncology: mind the heart. *Crit Rev Oncol Hematol*. 2005;53(2):101-113. doi:10.1016/j.critrevonc.2004.10.001

31. Chiong M, Wang Z v, Pedrozo Z, et al. Cardiomyocyte death: mechanisms and translational implications. *Cell Death Dis*. 2011;2(12):e244-e244. doi:10.1038/cddis.2011.130

32. Whelan RS, Kaplinskiy V, Kitsis RN. Cell Death in the Pathogenesis of Heart Disease: Mechanisms and Significance. *Annu Rev Physiol*. 2010;72(1):19-44. doi:10.1146/annurev.physiol.010908.163111

33. Davies JE. The pharmacological basis of therapeutics. *Occup Environ Med*. 2007;64(8):e2-e2. doi:10.1136/oem.2007.033902

34. Liu J, Tu D, Dancey J, et al. Quality of Life Analyses in a Clinical Trial of DPPE (tesmilifene) Plus Doxorubicin Versus Doxorubicin in Patients with Advanced or Metastatic Breast Cancer: NCIC CTG Trial MA.19. *Breast Cancer Res Treat*. 2006;100(3):263-271. doi:10.1007/s10549-006-9257-1

35. Julka PK, Chacko RT, Nag S, et al. A phase II study of sequential neoadjuvant gemcitabine plus doxorubicin followed by gemcitabine plus

cisplatin in patients with operable breast cancer: prediction of response using molecular profiling. *Br J Cancer*. 2008;98(8):1327-1335. doi:10.1038/sj.bjc.6604322

36. Mancuso A, Migliorino M, de Santis S, Saponiero A, de Marinis F. Correlation between anemia and functional/cognitive capacity in elderly lung cancer patients treated with chemotherapy. *Annals of Oncology*. 2006;17(1):146-150. doi:10.1093/annonc/mdj038

37. Skeel RT, Khleif SN. *Handbook of Cancer Chemotherapy*. Lippincott Williams & Wilkins; 2011.

38. Beijnen JH, Rosing H, de Vries PA, Underberg WJ. Stability of anthracycline antitumour agents in infusion fluids. *J Parenter Sci Technol*. 39(6):220-222.

39. Andrews PA, Brenner DE, Chou FT, Kubo H, Bachur NR. Facile and definitive determination of human adriamycin and daunoribicin metabolites by high-pressure liquid chromatography. *Drug Metab Dispos*. 8(3):152-156.

40. Barenholz Y, Amselem S, Goren D, et al. Stability of liposomal doxorubicin formulations: Problems and prospects. *Med Res Rev*. 1993;13(4):449-491. doi:10.1002/med.2610130404

41. Zhao L, Zhang B. Doxorubicin induces cardiotoxicity through upregulation of death receptors mediated apoptosis in cardiomyocytes. *Sci Rep*. 2017;7. doi:10.1038/srep44735

42. Gregoriadis G. TARGETING OF DRUGS: IMPLICATIONS IN MEDICINE. *The Lancet*. 1981;318(8240):241-247. doi:10.1016/S0140-6736(81)90486-4

43. Gabizon A, Peretz T, Sulkes A, et al. *SyStemic Administration of Doxorubicin-Containing Liposomes in Cancer Patients: A Phase I Study*. Vol 25.; 1989.

44. Goren D, Gabizon A, Barenholz Y. *The Influence of Physical Characteristics of Liposomes Containing Doxorubicin on Their Pharmacological Behavior*.; 1990.

45. Barenholz Y (Chezy). Doxil® — The first FDA-approved nano-drug: Lessons learned. *Journal of Controlled Release*. 2012;160(2):117-134. doi:10.1016/j.jconrel.2012.03.020

46. Gabizon A, Shmeeda H, Barenholz Y. *Pharmacokinetics of Pegylated Liposomal Doxorubicin Review of Animal and Human Studies*. Vol 42.; 2003.

47. Matsumura Y, Maeda H. A new concept for macromolecular therapeutics in cancer chemotherapy: mechanism of tumoritropic accumulation of proteins and the antitumor agent smancs. *Cancer Res*. 1986;46(12 Pt 1):6387-6392.

48. Maeda H, Bharate GY, Daruwalla J. Polymeric drugs for efficient tumor-targeted drug delivery based on EPR-effect. *European Journal of Pharmaceutics and Biopharmaceutics*. 2009;71(3):409-419. doi:10.1016/j.ejpb.2008.11.010

49. Peer D. *Harnessing RNAi Nanomedicine for Precision Therapy*.; 2014. http://www.molcelltherapies.com/content/2/1/5

50. Le NTT, Cao V du, Nguyen TNQ, Le TTH, Tran TT, Hoang Thi TT. Soy Lecithin-Derived Liposomal Delivery Systems: Surface Modification and Current Applications. *Int J Mol Sci*. 2019;20(19):4706. doi:10.3390/ijms20194706

51. Deamer DW, Prince RC, Crofts AR. The response of fluorescent amines to pH gradients across liposome membranes. *Biochimica et Biophysica Acta (BBA) - Biomembranes*. 1972;274(2):323-335. doi:10.1016/0005-2736(72)90180-0

52. Nichols JW, Deamer DW. Catecholamine uptake and concentration by liposomes maintaining pH gradients. *Biochimica et Biophysica Acta (BBA) - Biomembranes*. 1976;455(1):269-271. doi:10.1016/0005-2736(76)90169-3

53. Haran G, Cohen R, Bar LK, Barenholz Y. Transmembrane ammonium sulfate gradients in liposomes produce efficient and stable entrapment of amphipathic weak bases. *Biochimica et Biophysica Acta (BBA) - Biomembranes*. 1993;1151(2):201-215. doi:10.1016/0005-2736(93)90105-9

54. Y. Barenholz GH. Method of amphiphatic drug loading in liposomes by pH gradient. Published online 1993.

55. Lasic DD, Čeh B, Stuart MCA, Guo L, Frederik PM, Barenholz Y. Transmembrane gradient driven phase transitions within vesicles: lessons for drug delivery. *Biochimica et Biophysica Acta (BBA) - Biomembranes*. 1995;1239(2):145-156. doi:10.1016/0005-2736(95)00159-Z

56. Lasic DD, Frederik PM, Stuart MCA, Barenholz Y, McIntosh TJ. Gelation of liposome interior A novel method for drug encapsulation. *FEBS Lett*. 1992;312(2-3):255-258. doi:10.1016/0014-5793(92)80947-F

57. Wei X, Shamrakov D, Nudelman S, et al. Cardinal Role of Intraliposome Doxorubicin-Sulfate Nanorod Crystal in Doxil Properties and Performance. *ACS Omega*. 2018;3(3):2508-2517. doi:10.1021/acsomega.7b01235

58. Gabizon A, Catane R, Uziely B, et al. *Prolonged Circulation Time and Enhanced Accumulation in Malignant Exudates of Doxorubicin Encapsulated in Polyethylene-Glycol Coated Liposomes 1*. Vol 154.; 1994. http://aacrjournals.org/cancerres/article-pdf/54/4/987/2455853/crs0540040987.pdf

59. Lasic DD, Martin FJ, eds. *Stealth Liposomes*. CRC Press; 2018. doi:10.1201/9780203738412

60. Gordon AN, Fleagle JT, Guthrie D, Parkin DE, Gore ME, Lacave AJ. Recurrent Epithelial Ovarian Carcinoma: A Randomized Phase III Study of Pegylated Liposomal Doxorubicin Versus Topotecan. *Journal of Clinical Oncology*. 2001;19(14):3312-3322. doi:10.1200/JCO.2001.19.14.3312

61. Jiang W, Lionberger R, Yu LX. In vitro and in vivo characterizations of PEGylated liposomal doxorubicin. *Bioanalysis*. 2011;3(3):333-344. doi:10.4155/bio.10.204

62. Shaikh AY, Shih JA. Chemotherapy-Induced Cardiotoxicity. *Curr Heart Fail Rep*. 2012;9(2):117-127. doi:10.1007/s11897-012-0083-y

63. Mohan P, Rapoport N. Doxorubicin as a Molecular Nanotheranostic Agent: Effect of Doxorubicin Encapsulation in Micelles or Nanoemulsions on the Ultrasound-Mediated Intracellular Delivery and

Nuclear Trafficking. *Mol Pharm*. 2010;7(6):1959-1973. doi:10.1021/mp100269f

64. Chatterjee K, Zhang J, Honbo N, Karliner JS. Doxorubicin Cardiomyopathy. *Cardiology*. 2010;115(2):155-162. doi:10.1159/000265166

65. Karukstis KK, Thompson EHZ, Whiles JA, Rosenfeld RJ. Deciphering the fluorescence signature of daunomycin and doxorubicin. *Biophys Chem*. 1998;73(3):249-263. doi:10.1016/S0301-4622(98)00150-1

66. Chen NT, Wu CY, Chung CY, et al. Correction: Probing the Dynamics of Doxorubicin-DNA Intercalation during the Initial Activation of Apoptosis by Fluorescence Lifetime Imaging Microscopy (FLIM). *PLoS One*. 2012;7(11). doi:10.1371/annotation/4c43c8c8-0a4e-425b-a72f-74e84f6f3c28

67. Motlagh NSH, Parvin P, Ghasemi F, Atyabi F. Fluorescence properties of several chemotherapy drugs: doxorubicin, paclitaxel and bleomycin. *Biomed Opt Express*. 2016;7(6):2400. doi:10.1364/boe.7.002400

68. Duray PH, Cuono CB, Madri JA. Demonstration of cutaneous doxorubicin extravasation by rhodamine-filtered fluorescence microscopy. *J Surg Oncol*. 1986;31(1):21-25. doi:10.1002/jso.2930310104

69. Angeloni L, Smulevich G, Marzocchi MP. Absorption, fluorescence and resonance Raman spectra of adriamycin and its complex with DNA. *Spectrochim Acta A*. 1982;38(2):213-217. doi:10.1016/0584-8539(82)80199-2

70. Gallois L, Fiallo M, Garnier-Suillerot A. Comparison of the interaction of doxorubicin, daunorubicin, idarubicin and idarubicinol with large unilamellar vesicles. *Biochimica et Biophysica Acta (BBA) - Biomembranes*. 1998;1370(1):31-40. doi:10.1016/S0005-2736(97)00241-1

71. Karukstis KK, Thompson EHZ, Whiles JA, Rosenfeld RJ. Deciphering the fluorescence signature of daunomycin and doxorubicin. *Biophys Chem*. 1998;73(3):249-263. doi:10.1016/S0301-4622(98)00150-1

72. Htun T. A Negative Deviation from Stern–Volmer Equation in Fluorescence Quenching. *J Fluoresc*. 2004;14(2):217-222. doi:10.1023/B:JOFL.0000016294.96775.fd

73. Htun T. A Negative Deviation from Stern–Volmer Equation in Fluorescence Quenching. *J Fluoresc*. 2004;14(2):217-222. doi:10.1023/B:JOFL.0000016294.96775.fd

74. McLennan IJ, Lenkinski RE, Yanuka Y. A nuclear magnetic resonance study of the self-association of adriamycin and daunomycin in aqueous solution. *Can J Chem*. 1985;63(6):1233-1238. doi:10.1139/v85-210

75. Anand R, Malanga M, Manet I, et al. *Citric Acid–γ-Cyclodextrin Crosslinked Oligomers as Carriers for Doxorubicin Delivery Electronic Supplementary Information GLOBAL ANALYSIS OF EQUILIBRIUM SPECTROSCOPIC DATA*.; 2013.

76. Changenet-Barret P, Gustavsson T, Markovitsi D, Manet I, Monti S. Unravelling molecular mechanisms in the fluorescence spectra of doxorubicin in aqueous solution by femtosecond fluorescence spectroscopy. doi:10.1039/C2CP44056Cï

77. Michaelclarson, Gmitro AF, Utzinger U, et al. Using FDA-approved drugs as off-label fluorescent dyes for optical biopsies: From in silico design to ex vivo proof-of-concept. *Methods Appl Fluoresc*. 2021;9(3). doi:10.1088/2050-6120/ac0619

78. Shah S, Chandra A, Kaur A, et al. Fluorescence properties of doxorubicin in PBS buffer and PVA films. *J Photochem Photobiol B*. 2017;170:65-69. doi:10.1016/j.jphotobiol.2017.03.024

79. Burke TG, Tritton TR. Ligand self-association at the surface of liposomes: A complication during equilibrium-binding studies. *Anal Biochem*. 1984;143(1):135-140. doi:10.1016/0003-2697(84)90567-0

80. Burke TG, Israel M, Seshadri R, Doroshow JH. A fluorescence study examining how 14-valerate side chain substitution modulates anthracycline binding to small unilamellar phospholipid vesicles. *Biochimica et Biophysica Acta (BBA) - Biomembranes*. 1989;982(1):123-130. doi:10.1016/0005-2736(89)90182-X

81. Mati SS, Sarkar S, Sarkar P, Bhattacharya SC. Explicit Spectral Response of the Geometrical Isomers of a Bio-Active Pyrazoline Derivative Encapsulated in β-Cyclodextrin Nanocavity: A Photophysical and Quantum Chemical Analysis. *J Phys Chem A*. 2012;116(42):10371-10382. doi:10.1021/jp307964z

82. Fiallo M, Laigle A, Borrel MN, Garnier-Suillerot A. Accumulation of degradation products of doxorubicin and pirarubicin formed in cell culture medium within sensitive and resistant cells. *Biochem Pharmacol*. 1993;45(3):659-665. doi:10.1016/0006-2952(93)90140-R

83. Hovorka O, Šubr V, Větvička D, et al. Spectral analysis of doxorubicin accumulation and the indirect quantification of its DNA intercalation. *European Journal of Pharmaceutics and Biopharmaceutics*. 2010;76(3):514-524. doi:10.1016/j.ejpb.2010.07.008

84. Becker W. *The Bh TCSPC Technique - Principles and Applications*.; 2021. http://www.becker-hickl.com

85. Digman MA, Caiolfa VR, Zamai M, Gratton E. The Phasor Approach to Fluorescence Lifetime Imaging Analysis. *Biophys J*. 2008;94(2):L14-L16. doi:10.1529/biophysj.107.120154

86. Redford GI, Clegg RM. Polar Plot Representation for Frequency-Domain Analysis of Fluorescence Lifetimes. *J Fluoresc*. 2005;15(5):805-815. doi:10.1007/s10895-005-2990-8

87. Clayton AHA, Hanley QS, Verveer PJ. Graphical representation and multicomponent analysis of single-frequency fluorescence lifetime imaging microscopy data. *J Microsc*. 2004;213(1):1-5. doi:10.1111/j.1365-2818.2004.01265.x

88. Shah S, Chandra A, Kaur A, et al. Fluorescence properties of doxorubicin in PBS buffer and PVA films. *J Photochem Photobiol B*. 2017;170:65-69. doi:10.1016/j.jphotobiol.2017.03.024

89. Zhou T, Luo T, Song J, Qu J. Phasor–Fluorescence Lifetime Imaging Microscopy Analysis to Monitor Intercellular Drug Release from a pH-Sensitive Polymeric Nanocarrier. *Anal Chem*. 2018;90(3):2170-2177. doi:10.1021/acs.analchem.7b04511

90. Wei X, Shamrakov D, Nudelman S, et al. Cardinal Role of Intraliposome Doxorubicin-Sulfate Nanorod Crystal in Doxil Properties and Performance. *ACS Omega*. 2018;3(3):2508-2517. doi:10.1021/acsomega.7b01235

91. Zhu S, Ma L, Wang S, et al. Light-Scattering Detection below the Level of Single Fluorescent Molecules for High-Resolution Characterization of Functional Nanoparticles. *ACS Nano*. 2014;8(10):10998-11006. doi:10.1021/nn505162u

92. Basuki JS, Duong HTT, Macmillan A, et al. Using Fluorescence Lifetime Imaging Microscopy to Monitor Theranostic Nanoparticle Uptake and Intracellular Doxorubicin Release. *ACS Nano*. 2013;7(11):10175-10189. doi:10.1021/nn404407g

93. de Mello JC, Wittmann HF, Friend RH. An improved experimental determination of external photoluminescence quantum efficiency. *Advanced Materials*. 1997;9(3):230-232. doi:10.1002/adma.19970090308

94. Stair R, Schneider WE, Jackson JK. A New Standard of Spectral Irradiance. *Appl Opt*. 1963;2(11):1151. doi:10.1364/AO.2.001151

95. Ranjit S, Datta R, Dvornikov A, Gratton E. Multicomponent Analysis of Phasor Plot in a Single Pixel to Calculate Changes of Metabolic Trajectory in Biological Systems. *J Phys Chem A*. 2019;123(45):9865-9873. doi:10.1021/acs.jpca.9b07880

96. Tian Y, Bromberg L, Lin SN, Alan Hatton T, Tam KC. Complexation and release of doxorubicin from its complexes with pluronic P85-b-poly(acrylic acid) block copolymers. *Journal of Controlled Release*. 2007;121(3):137-145. doi:10.1016/j.jconrel.2007.05.010

97. Schilt Y, Berman T, Wei X, Barenholz Y, Raviv U. Using solution X-ray scattering to determine the high-resolution structure and morphology of PEGylated liposomal doxorubicin nanodrugs. *Biochimica et Biophysica Acta (BBA) - General Subjects*. 2016;1860(1):108-119. doi:10.1016/j.bbagen.2015.09.012

98. Martí A, Armengol X, Estelrich J, Hernández-Borrell J. Encapsulation of doxorubicin in neutral liposomes by passive methods: evidence of drug-

lipid interaction at neutral pH. *J Microencapsul*. 1991;9(2):191-200. doi:10.3109/02652049109021236

99. Mathivathanan L, Yang G, Leng F, Raptis RG. Crystal structure and conformational analysis of doxorubicin nitrate. *Acta Crystallogr E Crystallogr Commun*. 2018;74(3):400-405. doi:10.1107/S2056989018002955

100. Bonvin D, Aschauer U, Alexander DTL, et al. Protein Corona: Impact of Lymph Versus Blood in a Complex In Vitro Environment. *Small*. 2017;13(29):1700409. doi:10.1002/smll.201700409

101. Treuel L, Docter D, Maskos M, Stauber RH. Protein corona – from molecular adsorption to physiological complexity. *Beilstein Journal of Nanotechnology*. 2015;6:857-873. doi:10.3762/bjnano.6.88

102. Hamad-Schifferli K. Exploiting the novel properties of protein coronas: emerging applications in nanomedicine. *Nanomedicine*. 2015;10(10):1663-1674. doi:10.2217/nnm.15.6

103. Hajipour MJ, Laurent S, Aghaie A, Rezaee F, Mahmoudi M. Personalized protein coronas: a “key” factor at the nanobiointerface. *Biomater Sci*. 2014;2(9):1210. doi:10.1039/C4BM00131A

104. Pino P del, Pelaz B, Zhang Q, Maffre P, Nienhaus GU, Parak WJ. Protein corona formation around nanoparticles – from the past to the future. *Mater Horiz*. 2014;1(3):301-313. doi:10.1039/C3MH00106G

105. Tenzer S, Docter D, Kuharev J, et al. Rapid formation of plasma protein corona critically affects nanoparticle pathophysiology. *Nat Nanotechnol*. 2013;8(10):772-781. doi:10.1038/nnano.2013.181

106. Barrán-Berdón AL, Pozzi D, Caracciolo G, et al. Time Evolution of Nanoparticle–Protein Corona in Human Plasma: Relevance for Targeted Drug Delivery. *Langmuir*. 2013;29(21):6485-6494. doi:10.1021/la401192x

107. Kumar A, Bicer EM, Morgan AB, et al. Enrichment of immunoregulatory proteins in the biomolecular corona of nanoparticles within human respiratory tract lining fluid. *Nanomedicine*. 2016;12(4):1033-1043. doi:10.1016/j.nano.2015.12.369

108. Corbo C, Molinaro R, Taraballi F, et al. Unveiling the *in Vivo* Protein Corona of Circulating Leukocyte-like Carriers. *ACS Nano*. 2017;11(3):3262-3273. doi:10.1021/acsnano.7b00376

109. Digiacomo L, Cardarelli F, Pozzi D, et al. An apolipoprotein-enriched biomolecular corona switches the cellular uptake mechanism and trafficking pathway of lipid nanoparticles. *Nanoscale*. 2017;9(44):17254-17262. doi:10.1039/C7NR06437C

110. Caracciolo G. Clinically approved liposomal nanomedicines: lessons learned from the biomolecular corona. *Nanoscale*. 2018;10(9):4167-4172. doi:10.1039/C7NR07450F

111. Pozzi D, Colapicchioni V, Caracciolo G, et al. Effect of polyethyleneglycol (PEG) chain length on the bio–nano-interactions between PEGylated lipid nanoparticles and biological fluids: from nanostructure to uptake in cancer cells. *Nanoscale*. 2014;6(5):2782. doi:10.1039/c3nr05559k

112. Palchetti S, Colapicchioni V, Digiacomo L, et al. The protein corona of circulating PEGylated liposomes. *Biochimica et Biophysica Acta (BBA) - Biomembranes*. 2016;1858(2):189-196. doi:10.1016/j.bbamem.2015.11.012

113. Tasciotti E, Molinaro R, Taraballi F, et al. Effects of the protein corona on liposome–liposome and liposome–cell interactions . *Int J Nanomedicine*. 2016;Volume 11:3049-3063. doi:10.2147/IJN.S109059

114. Corbo C, Molinaro R, Tabatabaei M, Farokhzad OC, Mahmoudi M. Personalized protein corona on nanoparticles and its clinical implications. *Biomater Sci*. 2017;5(3):378-387. doi:10.1039/C6BM00921B

115. Hadjidemetriou M, Al-Ahmady Z, Kostarelos K. Time-evolution of in vivo protein corona onto blood-circulating PEGylated liposomal doxorubicin (DOXIL) nanoparticles. *Nanoscale*. 2016;8(13):6948-6957. doi:10.1039/C5NR09158F

116. Caracciolo G, Pozzi D, Capriotti AL, et al. The liposome–protein corona in mice and humans and its implications for in vivo delivery. *J Mater Chem B*. 2014;2(42):7419-7428. doi:10.1039/C4TB01316F

117. Caracciolo G, Farokhzad OC, Mahmoudi M. Biological Identity of Nanoparticles In Vivo : Clinical Implications of the Protein Corona. *Trends Biotechnol*. 2017;35(3):257-264. doi:10.1016/j.tibtech.2016.08.011

118. Caracciolo G, Palchetti S, Digiacomo L, et al. Human Biomolecular Corona of Liposomal Doxorubicin: The Overlooked Factor in Anticancer Drug Delivery. *ACS Appl Mater Interfaces*. 2018;10(27):22951-22962. doi:10.1021/acsami.8b04962

119. Pabst G, Koschuch R, Pozo-Navas B, Rappolt M, Lohner K, Laggner P. Structural analysis of weakly ordered membrane stacks. *J Appl Crystallogr*. 2003;36(6):1378-1388. doi:10.1107/S0021889803017527

120. Pozzi D, Colapicchioni V, Caracciolo G, et al. Effect of polyethyleneglycol (PEG) chain length on the bio–nano-interactions between PEGylated lipid nanoparticles and biological fluids: from nanostructure to uptake in cancer cells. *Nanoscale*. 2014;6(5):2782. doi:10.1039/c3nr05559k

121. Venditto VJ, Szoka FC. Cancer nanomedicines: So many papers and so few drugs! *Adv Drug Deliv Rev*. 2013;65(1):80-88. doi:10.1016/j.addr.2012.09.038

122. Kennedy MT, Pozharski E v., Rakhmanova VA, MacDonald RC. Factors Governing the Assembly of Cationic Phospholipid-DNA Complexes. *Biophys J*. 2000;78(3):1620-1633. doi:10.1016/S0006-3495(00)76714-2

123. Caracciolo G. Liposome–protein corona in a physiological environment: Challenges and opportunities for targeted delivery of nanomedicines. *Nanomedicine*. 2015;11(3):543-557. doi:10.1016/j.nano.2014.11.003

124. Quagliarini E, di Santo R, Pozzi D, Tentori P, Cardarelli F, Caracciolo G. Mechanistic insights into the release of doxorubicin from graphene oxide in cancer cells. *Nanomaterials*. 2020;10(8):1-11. doi:10.3390/nano10081482

125. Chung C, Kim YK, Shin D, Ryoo SR, Hong BH, Min DH. Biomedical Applications of Graphene and Graphene Oxide. *Acc Chem Res*. 2013;46(10):2211-2224. doi:10.1021/ar300159f

126. Liu J, Cui L, Losic D. Graphene and graphene oxide as new nanocarriers for drug delivery applications. *Acta Biomater*. 2013;9(12):9243-9257. doi:10.1016/j.actbio.2013.08.016

127. Liu Z, Robinson JT, Sun X, Dai H. PEGylated Nanographene Oxide for Delivery of Water-Insoluble Cancer Drugs. *J Am Chem Soc*. 2008;130(33):10876-10877. doi:10.1021/ja803688x

128. Sun X, Liu Z, Welsher K, et al. Nano-graphene oxide for cellular imaging and drug delivery. *Nano Res*. 2008;1(3):203-212. doi:10.1007/s12274-008-8021-8

129. Wu S, Zhao X, Li Y, et al. Adsorption Properties of Doxorubicin Hydrochloride onto Graphene Oxide: Equilibrium, Kinetic and Thermodynamic Studies. *Materials*. 2013;6(5):2026-2042. doi:10.3390/ma6052026

130. An SS, Wu SY, Hulme J. Current applications of graphene oxide in nanomedicine. *Int J Nanomedicine*. Published online August 2015:9. doi:10.2147/IJN.S88285

131. Dasari Shareena TP, McShan D, Dasmahapatra AK, Tchounwou PB. A Review on Graphene-Based Nanomaterials in Biomedical Applications and Risks in Environment and Health. *Nanomicro Lett*. 2018;10(3):53. doi:10.1007/s40820-018-0206-4

132. Stringari C, Cinquin A, Cinquin O, Digman MA, Donovan PJ, Gratton E. Phasor approach to fluorescence lifetime microscopy distinguishes different metabolic states of germ cells in a live tissue. *Proceedings of the National Academy of Sciences*. 2011;108(33):13582-13587. doi:10.1073/pnas.1108161108

133. Basuki JS, Duong HTT, Macmillan A, et al. Using Fluorescence Lifetime Imaging Microscopy to Monitor Theranostic Nanoparticle Uptake and Intracellular Doxorubicin Release. *ACS Nano*. 2013;7(11):10175-10189. doi:10.1021/nn404407g

134. Caccamo D, Currò M, Ientile R, et al. Intracellular Fate and Impact on Gene Expression of Doxorubicin/Cyclodextrin-Graphene Nanomaterials at Sub-Toxic Concentration. *Int J Mol Sci*. 2020;21(14):4891. doi:10.3390/ijms21144891

135. Zhang X, Shastry S, Bradforth SE, Nadeau JL. Nuclear uptake of ultrasmall gold-doxorubicin conjugates imaged by fluorescence lifetime imaging microscopy (FLIM) and electron microscopy. *Nanoscale*. 2015;7(1):240-251. doi:10.1039/C4NR04707A

136. Suarasan S, Craciun AM, Licarete E, Focsan M, Magyari K, Astilean S. Intracellular Dynamic Disentangling of Doxorubicin Release from Luminescent Nanogold Carriers by Fluorescence Lifetime Imaging Microscopy (FLIM) under Two-Photon Excitation. *ACS Appl Mater Interfaces*. 2019;11(8):7812-7822. doi:10.1021/acsami.8b21269

137. Oladejo M, Paterson Y, Wood LM. Clinical Experience and Recent Advances in the Development of Listeria-Based Tumor Immunotherapies. *Front Immunol*. 2021;12. doi:10.3389/fimmu.2021.642316

138. Stritzker J, Pilgrim S, Szalay AA, Goebel W. Prodrug converting enzyme gene delivery by L. monocytogenes. *BMC Cancer*. 2008;8(1):94. doi:10.1186/1471-2407-8-94

139. van Pijkeren JP, Morrissey D, Monk IR, et al. A Novel *Listeria monocytogenes* -Based DNA Delivery System for Cancer Gene Therapy. *Hum Gene Ther*. 2010;21(4):405-416. doi:10.1089/hum.2009.022

140. Wood LM, Paterson Y. Attenuated Listeria monocytogenes: a powerful and versatile vector for the future of tumor immunotherapy. *Front Cell Infect Microbiol*. 2014;4. doi:10.3389/fcimb.2014.00051

141. García-Heredia A, Pohane AA, Melzer ES, et al. Peptidoglycan precursor synthesis along the sidewall of pole-growing mycobacteria. *Elife*. 2018;7. doi:10.7554/eLife.37243

142. Yang M, Jalloh AS, Wei W, Zhao J, Wu P, Chen PR. Biocompatible click chemistry enabled compartment-specific pH measurement inside E. coli. *Nat Commun*. 2014;5(1):4981. doi:10.1038/ncomms5981

143. Rivera SL, Espaillat A, Aditham AK, et al. Chemically Induced Cell Wall Stapling in Bacteria. *Cell Chem Biol*. 2021;28(2):213-220.e4. doi:10.1016/j.chembiol.2020.11.006

144. Coleman JN, Lotya M, O'Neill A, et al. Two-Dimensional Nanosheets Produced by Liquid Exfoliation of Layered Materials. *Science (1979)*. 2011;331(6017):568-571. doi:10.1126/science.1194975

145. Wang K, Wang J, Fan J, et al. Ultrafast Saturable Absorption of Two-Dimensional MoS $_2$ Nanosheets. *ACS Nano*. 2013;7(10):9260-9267. doi:10.1021/nn403886t

146. He GS, Qin HY, Zheng Q. Rayleigh, Mie, and Tyndall scatterings of polystyrene microspheres in water: Wavelength, size, and angle dependences. *J Appl Phys*. 2009;105(2):023110. doi:10.1063/1.3068473

147. Stair R, Schneider WE, Jackson JK. A New Standard of Spectral Irradiance. *Appl Opt*. 1963;2(11):1151. doi:10.1364/AO.2.001151

Appendix A
Materials and Methods

Materials: Hydrogenated soybean phosphatidylcholine (HSPC), cholesterol, and DSPE-PEG2k were obtained from Avanti Polar Lipids (Alabaster, AL, USA). DOX hydrochloride (powder) was purchased from Sigma Aldrich (Milan, Italy). Doxoves® (F30204B-D) and the plain ammonium sulfate (AS) control liposomes (F30204B-C) were obtained from FormuMax Scientific (Sunnyvale, CA, USA). KI was obtained from Sigma Aldrich (Milan, Italy).

Preparations: DOX crystals-like nano-rods: to prepare DOX-sulfate crystals, a solution of DOX HCl (10 mg/mL) in water was added dropwise into a 2-mL solution of ammonium sulfate (500 mM, pH=5.5), under vigorous magnetic stirring; when the solution turns turbid the titration endpoint is reached and an insoluble precipitate is formed. The precipitate was transferred into a WillCo plate to rest until it was completely dry.DOX-loaded liposomes: DOX®-Like Nanoparticles (DLN) were prepared with the thin lipid film method. Briefly, HSPC, cholesterol and DSPE-PEG2k (56.3:38.4:5.3 mol%) were dissolved in chloroform. The organic solvent was then evaporated by rotary evaporation under a reduced pressure for 2-hours at room temperature. Multilamellar vesicles (MLVs) were formed by hydrating the lipid film for 3h at 50°C with 250 mM ammonium sulphate (AS) (pH: 5.4). The liposomal suspension was dialyzed by centrifugation for 30 min at 8900 rpm to remove AS (final lipid concentration, 1.5 mg/ml). The multilamellar liposomes were extruded using the Avanti mini extruder (40 passages through 100 nm pore-diameter filters) to obtain small unilamellar vesicles (SUVs). DOX hydrochloride was dissolved in 250 mM AS

(pH 7.4) (drug final concentration 0,15 mg/ml, i.e. 260 mM). The final step was adding DOX hydrochloride solution to SUVs to produce DOX-loaded SUVs. At the end, DLNs were of 1 mg/mL total lipids and 0.05 mg/mL total DOX (i.e. 86 mM). The DOX to lipid weight ratio used in the remote loading was maintained at 0.05.

Atomic Force Microscopy: Topographic measurements were performed employing a commercial Dimension Icon AFM (Bruker) operating in PeakForce Tapping™ (PFT) mode and using ScanAsyst™-air probes (nominal elastic constant $0.4\,\mathrm{N\ m^{-1}}$). PFT-mode imaging is performed by nano-indenting the sample pixel-by-pixel controlling the force applied by the tip.

Fluorescence Lifetime Imaging experiments and phasor analysis: FLIM was performed by using Leica TCS SP5 confocal microscope (Leica Microsystems, Mannheim, Germany). The samples were observed by a pulsed diode laser operating at 40 MHz with an excitation wavelength of 470 nm (the average power at the sample was 10-20 µW). The emission was collected in the wavelength range between 520 and 650 nm by a photomultiplier tube interfaced with a time correlated single photon counting (TCSPC) card (PicoHarp 300, PicoQuant, Berlin). The phasor analysis of experimental lifetime acquisitions was performed by using a dedicated routine of SimFCS software (Laboratory for Fluorescence Dynamics, University of California, Irvine). The phasor rules of composition are widely described in chapter 2.

Spin Coater: To destroy mechanically DOX® and DLN, samples were seeded on a glass Petri dish and then spin-coated for 1 min at 5000 rpm. The aqueous solution is naturally lost during the procedure. DOX crystals and/or membrane patches adhere directly on the glass.

Absorption and Fluorescence spectroscopy: to measure the absorption spectra in the UV-visible range it was used a spectrophotometer (mod. Lambda 950, Perkin Elmer) equipped with adequate holder for sample in solid state or in solution. The evaluation of the contribution of the optical scattering to the measured spectra was performed by fitting the data of the measured spectra in the long wavelength range (>700 nm) and in the interval 300-350 nm to a λ-b function [144,145]. The values of the parameter b resulting from the fitting is in the range of 1.9-2.1, in good agreement with literature[146]. The resulting scattering background is then subtracted from absorption spectra. In addition, an integration sphere (Labsphere) was used to measure the absorption spectra, following the protocol present in literature[94]. In brief, a calibrate broadband lamp was used to illuminate the samples[147] and the resulting spectra of optical signals collected by the integration sphere were measured by a fiber-coupled monochromator (mod. Flame, Ocean Optics). The integration sphere was also used for the absorption and the QY of DOX_f and DOX_c[94]. In brief the samples were optically stimulated by a diode laser (mod. L6Cc, Oxxius) at 488 nm, and a diode (LED) with emission peak at 470 nm was used fore the evaluation of the absorption. A fiber-coupled monochromator was used to measure the intensity of the excitation laser and of the fluorescence emitted by the samples. These procedures were executed in different configuration, following the protocols from literature[147]; in one configuration with the excitation laser hitting the inner surface of the integration sphere and without the sample in it (configuration hereafter denote as SL), another with the sample inside the sphere placed along the laser path (configuration hereafter denote as LonS) and out of the laser trajectory (configuration hereafter denote as LoutS). The intensity of the laser and of the photoluminescence measured were corrected for the spectral response of the detection system (tacking in account the reflectance of the sphere inner coating, the attenuation of the optical fiber, the detection efficiency of the instrument) and

for the cuvette contribution and substrate, and they were dived for their respective time of integration. The fraction of light absorbed by the samples (A_s) and the QY_{PL} (photoluminescence quantum yield) were measured as follow:

$$A_s = 1 - \frac{I_L^{LonS}}{I_L^{LoutS}} \qquad Eq.A.1$$

$$QY_{PL} == \frac{I_{PL}^{LonS} - (1 - A_s) I_{PL}^{LoutS}}{I_L^{SL} A_s} \qquad Eq.A.2$$

Where I_L and I_{PL} are, respectively, the corrected intensities of the laser and of the photoluminescence, in the different configuration.

For what concern the experiments of absorption and fluorescence carried out on DOX® and DLN in solution the spectra were recorded with 1-cm optical path (Hellma, Müllheim, Germany) at 23°C with a JASCO V550 spectrophotometer (JASCO, Easton, MD, USA) and with a Cary Eclipse spectrofluorometer (Variant, Palo Alto, CA, USA). All the samples (DLN, DOX® and DOX, used as reference material) were diluted in water and then the specter was measured. The fluorescence spectra were measured with an excitation wavelength of 470 nm, and the emission was integrated between 500 and 700 nm. UV-Vis spectra were corrected for the optical scattering by using a linear fit in the range of 350±10 and 580±10. The plot of absorbance (470 nm) vs fluorescence was fitted with linear regression. The ratio between the slope of DOX® (or (DLN) and the slope of DOX was used to derive the ratio between QYs. The absolute QYPL of the different liposomes was the calculate using the QY of DOX (4.23±0.09) that was measured independently.

Appendix B: Patent

The results of work described in Chapter 3 prompted us to protect the methodology through patenting it. Here below abstract and major patent claims are reported:

Abstract

The present invention relates to determination of supramolecular organization in a substance including target molecules and nanocarriers at least one of which is luminescent, based on a step of collecting of lifetime decay data of at least a standard substance pure or substantially pure wherein a known organization state of the target molecules and the nanocarriers is pure or substantially pure; and a step of comparing the standard data and test data from a test substance.

CLAIMS

1. Determination method of a supramolecular organization of target luminescent molecules encapsulated within nanocarrier particles by lifetime analysis comprising the steps of:

- defining at least a first putative standard supramolecular organization of a plurality of target luminescent molecules and/or the nanocarrier particles wherein the molecules and/or the nanocarrier particles are purely or nearly purely organized and optionally the nanocarrier particle is also luminescent;
- receiving at least a first standard luminescence lifetime dataset representing a first decay associated to a first standard substance where

the molecules and/or the nanocarrier particles are purely or nearly purely organized according to the first putative supramolecular organization;

- processing a test substance comprising nanocarriers with the target luminescent molecules to obtain a test luminescence lifetime dataset of the test substance comprising the target luminescent molecule having an unknown supramolecular organization;
- quantitatively comparing the test luminescence lifetime dataset and the at least first standard luminescence lifetime dataset;
- determining whether a second supramolecular organization of molecules and the nanocarrier particles is present or not in the test substance based on quantitative superimposition of the test and first standard luminescence lifetime dataset.

2. Determination method according to claim 1, wherein:

- said step of defining comprises at least a second or more putative standard supramolecular organizations of the target luminescent molecules;
- said step of receiving comprises a second or more standard luminescence lifetime dataset representing a second decay associated to a first standard substance where the molecules and/or the nanocarrier particles are purely or nearly purely organized according to the second or more putative organization; and
- the step of determining includes whether a further supramolecular organization of the target luminescent molecules and/or the nanocarrier particles is present in the test substance based on whether test substance luminescence lifetime data is a linear combination of the standard luminescence lifetime dataset.

3. Determination method according to claim 2, further comprising the steps of:

- Identifying a number of iterations for said two or more putative standard

supramolecular organization states;

- collecting comparison luminescence lifetime data from a comparison substance generated so as not to show at least one of said putative standard organization states of the target luminescent molecules and the nanocarrier particles; and
- comparing the test substance lifetime data and the comparison substance lifetime data to confirm whether the number of iterations indicates the total number of standard supramolecular organization states of the luminescent target molecules present within the test substance.

4. Method according to any of the preceding claims comprising an additional step of quantifying the fractional intensity contribution of each defined supramolecular organization of the target luminescent molecules and/or the nanocarrier.
5. Method according to any of the preceding claims, wherein said luminescence lifetime data are either fitted exponential decay data or phasor plot data.
6. Method according to claim 5, wherein fitting exponential decay comprises the calculation of a i-th weight Ai attributable to each i-th putative organization state and a i-th characteristic lifetime attributable to each i-th putative organization state is already assigned from the i-th standard luminescence lifetime dataset obtained in said step of receiving.
7. Method according to any of the previous claims, wherein the molecule or nanocarrier is a drug.
8. Method according to any of the preceding claims, wherein the standard luminescence lifetime data are mono-exponential.